A DIVERGENCE-FREE AND $H(DIV)$-CONFORMING EMBEDDED-HYBRIDIZED DG METHOD FOR THE INCOMPRESSIBLE RESISTIVE MHD EQUATIONS*

JAU-UEI CHEN† TAMÁS L. HORVÁTH‡ AND TAN BUI-THANH†§

Abstract. We present a divergence-free and $H(div)$-conforming hybridized discontinuous Galerkin (HDG) method and a computationally efficient variant called embedded-HDG (E-HDG) for solving stationary incompressible viso-resistive magnetohydrodynamic (MHD) equations. The proposed E-HDG approach uses continuous facet unknowns for the vector-valued solutions (velocity and magnetic fields) while it uses discontinuous facet unknowns for the scalar variable (pressure and magnetic pressure). This choice of function spaces makes E-HDG computationally far more advantageous, due to the much smaller number of degrees of freedom, compared to the HDG counterpart. The benefit is even more significant for three-dimensional/high-order/fine mesh scenarios. On simplicial meshes, the proposed methods with a specific choice of approximation spaces are well-posed for linear(ized) MHD equations. For nonlinear MHD problems, we present a simple approach exploiting the proposed linear discretizations by using a Picard iteration. The beauty of this approach is that the divergence-free and $H(div)$-conforming properties of the velocity and magnetic fields are automatically carried over for nonlinear MHD equations. We study the accuracy and convergence of our E-HDG method for both linear and nonlinear MHD cases through various numerical experiments, including two- and three-dimensional problems with smooth and singular solutions. The numerical examples show that the proposed methods are pressure robust, and the divergence of the resulting velocity and magnetic fields is machine zero for both smooth and singular problems.

Key words. hybridized discontinuous Galerkin, embedded-hybridized discontinuous Galerkin, resistive magnetohydrodynamics, Stokes equations, Maxwell equations

AMS subject classifications. 65N30, 76W05

1. Introduction.

Magnetohydrodynamics (MHD) is a field within continuum mechanics that investigates the behavior of electrically conducting fluids in the presence of magnetic fields [32]. This coupled phenomenon holds significant importance across various fields including astrophysics [48, 49], planetary magnetism [20, 63], nuclear engineering [76, 42, 90], and metallurgical industry [1, 31]. This paper considers the standard form of the stationary incompressible MHD equations [5, 44, 45, 51]. Specifically, ignoring the effects related to high-frequency phenomena and convection current, and focusing on a medium that is non-polarizable, non-magnetizable, and homogeneous, the resulting MHD equations read

$$-\frac{1}{\mathrm{Re}}\Delta \boldsymbol{u} + \nabla p + (\boldsymbol{u}\cdot\nabla)\boldsymbol{u} + \kappa \boldsymbol{b}\times(\nabla\times\boldsymbol{b}) = \boldsymbol{g}, \tag{1.1a}$$

$$\nabla\cdot\boldsymbol{u} = 0, \tag{1.1b}$$

$$\frac{\kappa}{\mathrm{Rm}}\nabla\times(\nabla\times\boldsymbol{b}) + \nabla r - \kappa\nabla\times(\boldsymbol{u}\times\boldsymbol{b}) = \boldsymbol{f}, \tag{1.1c}$$

$$\nabla\cdot\boldsymbol{b} = 0, \tag{1.1d}$$

*

†Department of Aerospace Engineering and Engineering Mechanics, The University of Texas at Austin, Austin, TX 78712, USA (chenju@itexas.edu).

‡Department of Mathematics and Statistics, Oakland University, Rochester, MI 48309, USA (thorvath@oakland.edu).

§Oden Institute for Computational Engineering and Sciences, The University of Texas at Austin, Austin, TX 78712, USA (tanbui@oden.utexas.edu).

where $\boldsymbol{u}$ is the velocity of the fluid (plasma or liquid metal), $\boldsymbol{b}$ the magnetic field, p the fluid pressure, and r a Lagrange multiplier[1] that is associated with the divergence constraint (1.1d) on $\boldsymbol{b}$. The system (1.1) is characterized by three dimensionless parameters: the fluid Reynolds number $\mathrm{Re} > 0$, the magnetic Reynolds number $\mathrm{Rm} > 0$, and the coupling parameter $\kappa = \mathrm{Ha}^2/(\mathrm{ReRm})$, with the Hartmann number $\mathrm{Ha} > 0$. For a more detailed exploration of these parameters, we refer to [5, 45, 32].

The major challenges in the discretization of the MHD equations are the following: (i) multi-physics with disparate temporal (for the time-dependent MHD equations) and spatial scales; (ii) nonlinearity; (iii) incompressibility. The satisfaction of exact mass conservation in (1.1b) is closely tied to the concept of *pressure-robustness*, which is the statement about the independence between the magnitude of the pressure error and the *a priori* error estimate for the velocity [73, 74, 59]. Without global enforcement of the continuity equation pointwise, large velocity error can be induced by large pressure error. By global enforcement, we mean that the jump of the normal component of velocity has to vanish across the interior boundaries of elements on a given mesh. In other words, the approximation of velocity $\boldsymbol{u}_h$ is desired to be in the $H(div)$ space in addition to $\nabla \cdot \boldsymbol{u}_h = 0$, where the divergence operator is defined in a weak sense. The definition of the $H(div)$ space and weak derivative will be elaborated in Section 2; (iv) The solenoidal constraint for the magnetic field. The violation of this constraint will cause the wrong topologies of magnetic field lines, leading to plasma transport in an incorrect direction. Furthermore, nonphysical forces proportional to the divergence error could be created, potentially inducing instability [19, 11, 91]; and (v) The dual saddle-point structure of the velocity-pressure. The discretized system is subject to having a notorious large conditional number and is thus difficult to solve.

Many numerical schemes have been proposed to solve linear, nonlinear, time-dependent, and -independent MHD systems. Regarding spatial discretization, hybridized discontinuous Galerkin (HDG) methods have demonstrated remarkable success [69, 23, 83, 64, 47, 77]. The HDG methods were first introduced under the context of symmetric elliptic problems [25] to overcome the common criticism had by discontinuous Galerkin (DG) methods on the significantly more globally coupled unknowns than continuous Galerkin methods due to the duplication of degrees of freedoms (DOFs) on element boundaries [24]. The HDG methods reduce the computational cost of DG methods by introducing facet variables uniquely defined on the intersections of element boundaries and removing local (element-wise) DOFs through static condensation, which was initially used in mixed finite element methods (i.e.,[16]). Once the facet variables are solved, the element DOFs can be recovered element-by-element in a completely embarrassing parallel fashion. Consequently, HDG methods are more efficient while retaining the attractive features of DG methods, such as being highly suitable for solving convection-dominated problems in complex geometries, delivering high-order accuracy in approximations, and accommodating h/p refinement [54].

The computational cost of HDG methods can be further lowered by using continuous facet variables across the skeleton of the mesh instead of the discontinuous ones used in HDG methods. This approach led to the embedded discontinuous Galerkin (EDG) methods and was first proposed for solving elliptic problems in [53]. Later, the EDG methods were developed for solving both compressible flow problems in [80, 79, 40] and incompressible flow problems in [65, 66]. All works showed that the method inherited many of the desirable features of DG methods. At the same time, the required number of DOFs was less than those of HDG methods and close to those

[1] Sometimes, this variable is also referred to as the magnetic pressure.

of continuous Galerkin (CG) methods on a given mesh. Further, the stiffness matrix arising from EDG discretization of the flow problems will have a similar sparsity structure as that of the statically condensed CG method [80, 79]. Unfortunately, employing the EDG method can compromise the conservative property. As a consequence, the EDG methods may lose the optimal converge property of the flux that distinguishes other HDG methods. [80, 79]. In particular, for the incompressible flow model, the velocity field cannot be globally divergence-free, and the mass can only be conserved in the local sense [66]. To strike a balance between HDG and EDG methods, an embedded-hybridized discontinuous Galerkin (E-HDG) method was first developed in [87] for the Stokes equations. The method is proved to be globally divergence-free and $H(div)$-conforming. The number of globally coupled DOFs can be substantially reduced by using a continuous basis for the facet velocity field while maintaining a discontinuous basis for the facet pressure. The methodology was later adopted to space-time discretization to solve incompressible flows on moving domains [55, 56] and is proved to be globally mass conserving, locally momentum conserving, and energy-stable.

Several approaches have been suggested to address the issue of the divergence-free constraint on the velocity field within the framework of DG, HDG, or E-HDG methods. An approach to overcome the issue is to use $H(div)$-conforming elements in the approximation of velocity, as discussed in [28, 50, 43] for DG methods. Alternatively, the constraint can be satisfied locally using solenoidal approximation space for DG methods [8, 60, 72, 94, 62] and globally for HDG methods [21]. On the other hand, $H(div)$-conformity can be acquired with the help of facet variables and proper design of numerical flux for HDG [70, 71, 85, 67, 86, 81, 47] and E-HDG [87, 55, 56] methods. Another technique to obtain globally divergence-free methods is to perform post-processing using special projection operators [14, 27, 92, 29, 78, 26, 30, 52, 68]. It is worthy to mention that in HDG methods the new velocity approximation obtained by the local post-processing is not only exactly divergence-free and $H(div)$-conforming but also has superconvergece property [78, 26]. One can also apply pressure-correction methods that relies on Helmholtz decomposition to maintain the divergence-free constraint [18, 61].

We remark that the divergence-free constraint on the magnetic field given in (1.1d) can be implied by the initial condition in the context of time-dependent MHD equations on the continuous level, and it is also known as the solenoidal involution property of the magnetic field. However, temporal and spatial discretization errors can destroy such a property. Numerous methods have been proposed to satisfy the $\nabla \cdot \boldsymbol{b} = 0$ constraint in MHD calculations, and some of the ideas can be linked to the approaches developed to handle the $\nabla \cdot \boldsymbol{u} = 0$ constraint in the context of solving incompressible flow problems. These methods include source term methods [82, 58], projection method [19, 34] (similar to the projection-correction methods [18, 61]), hyperbolic divergence cleaning methods [33, 62, 17, 23] (similar to artificial compressibility methods [12, 13]), locally divergence-free methods [72, 94] (use locally solenoidal approximation space and is similar to [8, 60, 62]), globally divergence-free methods [43] (use globally solenoidal approximation space), and constrained transport (CT) methods [38, 11, 75, 91]. Another approach to obtain a divergence-free and $H(div)$-conforming method was developed in [47], using an HDG method that hybridizes the facet Lagrange multiplier variable as well.

In this paper, we devise HDG and E-HDG methods, which are both divergence-free and $H(div)$-conforming, for solving the stationary incompressible viso-resistive MHD equations given in (1.1). *Though both approaches are constructed in parallel,*

our exposition will focus on E-HDG. We obtain $H(div)$-conformity by following an idea similar to [87, 55] and [47] through hybridization via a facet pressure and a facet Lagrange multiplier field using discontinuous facet functions. For the E-HDG variant, we use continuous facet functions for the velocity and the magnetic fields. Moreover, we extended the work in [69] and employed an upwind type numerical flux that is based on the first-order form of the linearized MHD system. This is in contrast to the work in [47] where the authors hybridized another popular class of DG methods called interior penalty discontinuous Galerkin (IPDG) methods [35, 7, 93, 6, 8] to construct the divergence-free and divergence-conforming HDG method for the time-dependent incompressible viso-resistive MHD equations. To ensure stability, the penalty parameter in IPDG methods, such as the one in typical Nitsche methods, must be sufficiently large. However, no analytically proven bound is available for this penalty parameter. Conversely, our approaches do not suffer from such difficulty, and the criteria of the stabilization parameters are well-defined. With a few assumptions, our proposed schemes are well-posed. The resulting E-HDG discretization for the linearized MHD model can be incorporated into a Picard iteration to construct a fully nonlinear solver provided it converges. This approach ensures that the divergence-free and $H(div)$-conforming properties still hold for the nonlinear case. Moreover, all results we discussed in the context of our E-HDG method are still applied to the HDG counterpart, including well-posedness, divergence-free property, and $H(div)$-conformity.

The paper is organized as follows. Section 2 outlines the notations. Section 3 proposes both the HDG and E-HDG discrtizatinos for the linearized incompressible viso-resistive MHD equations. In addition, the well-posedness of both methods is proven. Further, we prove the divergence-free property and $H(div)$-conformity of both the velocity (i.e., pointwise mass conservation) and the magnetic (i.e., pointwise absence of magnetic monopoles) fields for linear and nonlinear cases. The implementation aspect is discussed in Section 4, where we also compare the computational costs required by HDG and E-HDG methods. Several numerical examples for linear and nonlinear incompressible viso-resistive MHD equations are presented to demonstrate the accuracy and convergence of our proposed methods in both two- and three-dimensional settings. Section 5 concludes the paper with future work.

2. Notations. In this section, we introduce common notations and conventions to be used in the rest of the paper. Let $\Omega \subset \mathbb{R}^d$, $d = 2, 3$, be a bounded domain such that it is simply connected, and its boundary $\partial\Omega$ is a Lipschitz manifold with only one component. Suppose that we have a triangulation of Ω consisting of a finite number of nonoverlapping d-dimensional simplices, i.e., triangles for two dimensions and tetrahedra for three dimensions, respectively. We assume that the triangulation is shape-regular, i.e., for all d-dimensional simplices in the triangulation, the ratio of the diameter of the simplex and the radius of an inscribed d-dimensional ball is uniformly bounded. We will use Ω_h and $\mathcal{E}_h$ to denote the sets of d- and $(d-1)$-dimensional simplices of the triangulation and call $\mathcal{E}_h$ the mesh skeleton of the triangulation. The boundary and interior mesh skeletons are defined by $\mathcal{E}_h^\partial := \{e \in \mathcal{E}_h : e \subset \partial\Omega\}$ and $\mathcal{E}_h^o := \mathcal{E}_h \backslash \mathcal{E}_h^\partial$. We also define $\partial\Omega_h := \{\partial K : K \in \Omega_h\}$. The mesh size of triangulations is $h := \max_{K\in\Omega_h} \mathrm{diam}(K)$.

We use $(\cdot,\cdot)_D$ (respectively $\langle\cdot,\cdot\rangle_D$) to denote the L^2-inner product on a d- (respectively $(d-1)$-) dimensional domain D. The standard notation $W^{s,p}(D)$, $s \geq 0$, $1 \leq p \leq \infty$, is used for the Sobolev space on D based on L^p-norm with differentiability s (see, e.g., [39]) and $\|\cdot\|_{W^{s,p}(D)}$ denotes the associated norm. In particular, if $p = 2$,

we use $H^s(D) := W^{s,2}(D)$ and $\|\cdot\|_{s,D}$. $W^{s,p}(\Omega_h)$ denotes the space of functions whose restrictions on K reside in $W^{s,p}(K)$ for each $K \in \Omega_h$ and its norm is $\|u\|^p_{W^{s,p}(\Omega_h)} := \sum_{K\in\Omega_h} \|u|_K\|^p_{W^{s,p}(K)}$ if $1 \le p < \infty$ and $\|u\|_{W^{s,\infty}(\Omega_h)} := \max_{K\in\Omega_h} \|u|_K\|_{W^{s,\infty}(K)}$. For simplicity, we use $(\cdot,\cdot)$, $\langle\cdot,\cdot\rangle$, $\|\cdot\|_s$, $\|\cdot\|_{\partial\Omega_h}$, and $\|\cdot\|_{W^{s,\infty}}$ for $(\cdot,\cdot)_\Omega$, $\langle\cdot,\cdot\rangle_{\partial\Omega_h}$, $\|\cdot\|_{s,\Omega}$, $\|\cdot\|_{0,\partial\Omega_h}$, and $\|\cdot\|_{W^{s,\infty}(\Omega_h)}$, respectively.

For vector- or matrix-valued functions these notations are naturally extended with a component-wise inner product. We define similar spaces (respectively inner products and norms) on a single element and a single skeleton face/edge by replacing Ω_h with K and $\mathcal{E}_h$ with e. We define the gradient of a vector, the divergence of a matrix, and the outer product symbol $\otimes$ as:

$$(\nabla \boldsymbol{u})_{ij} = \frac{\partial u_i}{\partial x_j}, \quad (\nabla\cdot\boldsymbol{L})_i = \nabla\cdot\boldsymbol{L}(i,:) = \sum_{j=1}^{d} \frac{\partial \boldsymbol{L}_{ij}}{\partial x_j}, \quad (\boldsymbol{a}\otimes\boldsymbol{b})_{ij} = a_i b_j = \left(\boldsymbol{a}\boldsymbol{b}^T\right)_{ij}.$$

The curl of a vector when $d = 3$ takes its standard form, $(\nabla\times\boldsymbol{b})_i = \sum_{j,k} \varepsilon_{ijk} \frac{\partial \boldsymbol{b}_k}{\partial x_j}$, where ε is the Levi-Civita symbol. When $d = 2$, let us explicitly define the curl of a vector as the scalar quantity $\nabla\times\boldsymbol{b} = \frac{\partial \boldsymbol{b}_2}{\partial x_1} - \frac{\partial \boldsymbol{b}_1}{\partial x_2}$, and the curl of a scalar as the vector quantity $\nabla\times a = \left(\frac{\partial a}{\partial x_2}, -\frac{\partial a}{\partial x_1}\right)$. In this paper, $\boldsymbol{n}$ denotes a unit outward normal vector field on faces/edges. If $\partial K^- \cap \partial K^+ \in \mathcal{E}_h$ for two distinct simplices K^-, K^+, then $\boldsymbol{n}^-$ and $\boldsymbol{n}^+$ denote the outward unit normal vector fields on ∂K^- and ∂K^+, respectively, and $\boldsymbol{n}^- = -\boldsymbol{n}^+$ on $\partial K^- \cap \partial K^+$. We simply use $\boldsymbol{n}$ to denote either $\boldsymbol{n}^-$ or $\boldsymbol{n}^+$ in an expression that is valid for both cases, and this convention is also used for other quantities (restricted) on a face/edge $e \in \mathcal{E}_h$. We also define $\boldsymbol{N} := \boldsymbol{n}\otimes\boldsymbol{n}$ and $\boldsymbol{T} := \boldsymbol{I} - \boldsymbol{N}$. For a scalar quantity u which is double-valued on $e := \partial K^- \cap \partial K^+$, the jump term on e is defined by $[\![u\boldsymbol{n}]\!]|_e = u^+\boldsymbol{n}^+ + u^-\boldsymbol{n}^-$ where u^+ and u^- are the traces of u from K^+- and K^--sides, respectively. For double-valued vector quantity $\boldsymbol{u}$ and matrix quantity $\boldsymbol{L}$, jump terms are $[\![\boldsymbol{u}\cdot\boldsymbol{n}]\!]|_e = \boldsymbol{u}^+\cdot\boldsymbol{n}^+ + \boldsymbol{u}^-\cdot\boldsymbol{n}^-$, $[\![\boldsymbol{u}\times\boldsymbol{n}]\!]|_e = \boldsymbol{u}^+\times\boldsymbol{n}^+ + \boldsymbol{u}^-\times\boldsymbol{n}^-$, and $[\![\boldsymbol{L}\boldsymbol{n}]\!]|_e = \boldsymbol{L}^+\boldsymbol{n}^+ + \boldsymbol{L}^-\boldsymbol{n}^-$ where $\boldsymbol{L}\boldsymbol{n}$ denotes the matrix-vector product.

We define $\mathcal{P}_k(K)$ as the space of polynomials of degree at most k on K, with $k \ge 0$, and we define

$$\mathcal{P}_k(\Omega_h) := \left\{u \in L^2(\Omega) \ : \ u|_K \in \mathcal{P}_k(K) \ \forall K \in \Omega_h\right\}.$$

The space of polynomials on the mesh skeleton $\mathcal{P}_k(\mathcal{E}_h)$ is similarly defined, and their extensions to vector- or matrix-valued polynomials $[\mathcal{P}_k(\Omega_h)]^d$, $[\mathcal{P}_k(\Omega_h)]^{d\times d}$, $[\mathcal{P}_k(\mathcal{E}_h)]^d$, etc, are straightforward.

Finally, we use the usual definition of the $H(div)$- and $H(curl)$-conforming spaces, which are typical for mixed methods, and for methods dealing with electromagnetism, see [37, 16],

$$H(div,\Omega) := \left\{\boldsymbol{u} \in \left[L^2(\Omega)\right]^d \ : \ \nabla\cdot\boldsymbol{u} \in L^2(\Omega)\right\},$$

$$H(curl,\Omega) := \left\{\boldsymbol{u} \in \left[L^2(\Omega)\right]^d \ : \ \nabla\times\boldsymbol{u} \in \left[L^2(\Omega)\right]^{\tilde{d}}\right\}, \tag{2.1}$$

where $\tilde{d} = 3$ if $d = 3$, $\tilde{d} = 1$ if $d = 2$. In addition, the divergence $\nabla\cdot(\cdot)$ and curl $\nabla\times(\cdot)$ operators should be thought of in the weak sense (an extension of weak derivative defined in Definition 2.3 in [37]). Note that the jump condition $[\![\boldsymbol{u}\cdot\boldsymbol{n}]\!]|\, e = 0$ and $[\![\boldsymbol{u}\times\boldsymbol{n}]\!]|\, e = 0$ is necessary for ensuring $\boldsymbol{u} \in H(div,\Omega)$ and $\boldsymbol{u} \in H(curl,\Omega)$, respectively (Theorem 18.10 in [37]).

3. An E-HDG Formulation. First, consider the following incompressible viso-resistive MHD system linearized from Eq. (1.1)

$$-\frac{1}{\mathrm{Re}}\Delta \boldsymbol{u} + \nabla p + (\boldsymbol{w}\cdot\nabla)\boldsymbol{u} + \kappa \boldsymbol{d}\times(\nabla\times\boldsymbol{b}) = \boldsymbol{g}, \tag{3.1a}$$

$$\nabla\cdot\boldsymbol{u} = 0, \tag{3.1b}$$

$$\frac{\kappa}{\mathrm{Rm}}\nabla\times(\nabla\times\boldsymbol{b}) + \nabla r - \kappa\nabla\times(\boldsymbol{u}\times\boldsymbol{d}) = \boldsymbol{f}, \tag{3.1c}$$

$$\nabla\cdot\boldsymbol{b} = 0. \tag{3.1d}$$

Here, $\boldsymbol{d}$ is a prescribed magnetic field and $\boldsymbol{w}$ is a prescribed velocity field. From this point forward, we assume (see, e.g., [22, 57] for similar assumptions) $\boldsymbol{d}\in\left[W^{1,\infty}(\Omega)\right]^d$, $\boldsymbol{w}\in\left[W^{1,\infty}(\Omega_h)\right]^d\cap H(div,\Omega)$, $\nabla\cdot\boldsymbol{w}=0$ and $\boldsymbol{g},\boldsymbol{f}\in\left[L^2(\Omega)\right]^d$.

To apply the upwind type of numerical flux based on the work [69], we cast (3.1) into a first-order form by introducing auxiliary variables $\boldsymbol{L}$ and $\boldsymbol{J}$,

$$\mathrm{Re}\boldsymbol{L} - \nabla\boldsymbol{u} = \boldsymbol{0}, \tag{3.2a}$$

$$-\nabla\cdot\boldsymbol{L} + \nabla p + (\boldsymbol{w}\cdot\nabla)\boldsymbol{u} + \kappa\boldsymbol{d}\times(\nabla\times\boldsymbol{b}) = \boldsymbol{g}, \tag{3.2b}$$

$$\nabla\cdot\boldsymbol{u} = 0, \tag{3.2c}$$

$$\frac{\mathrm{Rm}}{\kappa}\boldsymbol{J} - \nabla\times\boldsymbol{b} = \boldsymbol{0}, \tag{3.2d}$$

$$\nabla\times\boldsymbol{J} + \nabla r - \kappa\nabla\times(\boldsymbol{u}\times\boldsymbol{d}) = \boldsymbol{f}, \tag{3.2e}$$

$$\nabla\cdot\boldsymbol{b} = 0, \tag{3.2f}$$

with Dirichlet boundary conditions

$$\boldsymbol{u} = \boldsymbol{u}_D, \quad \boldsymbol{b} := \boldsymbol{b}_D, \quad r = 0 \qquad \text{on } \partial\Omega. \tag{3.3}$$

In addition, we require the compatibility condition for $\boldsymbol{u}_D$ and the mean-value zero condition for p:

$$\langle \boldsymbol{u}_D\cdot\boldsymbol{n}, 1\rangle_{\partial\Omega} = 0, \qquad (p,1)_\Omega = 0. \tag{3.4}$$

To achieve $H(div)$-conforming property, we introduce constant parameters $\alpha_1,\beta_1,\beta_2\in\mathbb{R}$, and define the numerical flux inspired by the work [69] as

$$\begin{bmatrix} \hat{\boldsymbol{F}}^1\cdot\boldsymbol{n} \\ \hat{\boldsymbol{F}}^2\cdot\boldsymbol{n} \\ \hat{\boldsymbol{F}}^3\cdot\boldsymbol{n} \\ \hat{\boldsymbol{F}}^4\cdot\boldsymbol{n} \\ \hat{\boldsymbol{F}}^5\cdot\boldsymbol{n} \\ \hat{\boldsymbol{F}}^6\cdot\boldsymbol{n} \end{bmatrix} = \begin{bmatrix} -\hat{\boldsymbol{u}}\otimes\boldsymbol{n} \\ -\boldsymbol{L}\boldsymbol{n} + m\boldsymbol{u} + \hat{p}\boldsymbol{n} + \frac{1}{2}\kappa\boldsymbol{d}\times\left(\boldsymbol{n}\times\left(\boldsymbol{b}+\hat{\boldsymbol{b}}\right)\right) + \alpha_1(\boldsymbol{u}-\hat{\boldsymbol{u}}) \\ \boldsymbol{u}\cdot\boldsymbol{n} \\ -\boldsymbol{n}\times\hat{\boldsymbol{b}} \\ \boldsymbol{n}\times\boldsymbol{J} + \hat{r}\boldsymbol{n} - \frac{1}{2}\kappa\boldsymbol{n}\times((\boldsymbol{u}+\hat{\boldsymbol{u}})\times\boldsymbol{d}) + (\beta_1\boldsymbol{T}+\beta_2\boldsymbol{N})\left(\boldsymbol{b}-\hat{\boldsymbol{b}}\right) \\ \boldsymbol{b}\cdot\boldsymbol{n} \end{bmatrix}, \tag{3.5}$$

where $m := \boldsymbol{w}\cdot\boldsymbol{n}$. It should be noted that $\hat{\boldsymbol{u}}$, $\hat{p}$, $\hat{\boldsymbol{b}}$, and $\hat{r}$ are the restrictions (or traces) of $\boldsymbol{u}$, p, $\boldsymbol{b}$, and r on $\mathcal{E}_h$. These $\hat{\boldsymbol{u}}$, $\hat{p}$, $\hat{\boldsymbol{b}}$, and $\hat{r}$ will be regarded as unknowns in discretizations to obtain an E-HDG method. It will be shown that the conditions $\alpha_1 > \frac{1}{2}\|\boldsymbol{w}\|_{L^\infty}$, and $\beta_1\boldsymbol{T}+\beta_2\boldsymbol{N} > 0$[2] are sufficient for the well-posedness of our E-HDG formulation. Note that all 6 components of the E-HDG flux, $\hat{\boldsymbol{F}}$, for simplicity

[2]The sign of "greater than" here means that the matrix (or the second order tensor) $\beta_1\boldsymbol{T}+\beta_2\boldsymbol{N}$ is positive definite.

are denoted in the same fashion (by a bold italic symbol). It is, however, clear from (3.2) that $\hat{\boldsymbol{F}}^1$ is a third order tensor, $\hat{\boldsymbol{F}}^2$ is a second order tensor, $\hat{\boldsymbol{F}}^3$ is a vector, etc, and that the normal E-HDG flux components, $\hat{\boldsymbol{F}}^i \cdot \boldsymbol{n}$ in (3.5), are tensors of one order lower.

For discretization, we introduce the discontinuous piecewise and the continuous polynomial spaces

$$\mathbf{G}_h := [\mathcal{P}_k(\Omega_h)]^{d\times d}, \qquad \mathbf{V}_h := [\mathcal{P}_k(\Omega_h)]^{d}, \qquad \mathbf{Q}_h := \mathcal{P}_{\overline{k}}(\Omega_h),$$

$$\mathbf{H}_h := [\mathcal{P}_k(\Omega_h)]^{\tilde{d}}, \qquad \mathbf{C}_h := [\mathcal{P}_k(\Omega_h)]^{d}, \qquad \mathbf{S}_h := \mathcal{P}_{\overline{k}}(\Omega_h), \qquad \mathbf{M}_h := [\mathcal{P}_k(\mathcal{E}_h)\cap\mathcal{C}(\mathcal{E}_h)]^{d},$$

$$\mathbf{P}_h := [\mathcal{P}_k(\mathcal{E}_h)], \qquad \mathbf{\Lambda}_h := [\mathcal{P}_k(\mathcal{E}_h)\cap\mathcal{C}(\mathcal{E}_h)]^{d}, \qquad \mathbf{\Gamma}_h := [\mathcal{P}_k(\mathcal{E}_h)],$$

where $\overline{k} := k-1$, $\mathcal{C}(\mathcal{E}_h)$ is the continuous function space defined on the mesh skeleton, and $\tilde{d}$ is defined in (2.1).

REMARK 1. *The functions in $\mathbf{M}_h$ and $\mathbf{\Lambda}_h$ are used to approximate the traces of the velocity and the magnetic field, respectively. By a slight modification of these spaces (i.e., $\mathbf{M}_h := [\mathcal{P}_k(\mathcal{E}_h)]^d$ and $\mathbf{\Lambda}_h := [\mathcal{P}_k(\mathcal{E}_h)]^d$), a divergence-free and $H(div)$-conforming HDG method can be obtained. All the results presented in Sections 3.1, 3.2 and 3.3 can be directly applied to the resulting HDG method. In addition, we will numerically compare the computational time needed by HDG and E-HDG methods in Section 4.*

Let us introduce two identities which are useful throughout the paper:

$$(\boldsymbol{u}, \boldsymbol{d}\times(\nabla\times\boldsymbol{b}))_K = (\boldsymbol{b}, \nabla\times(\boldsymbol{u}\times\boldsymbol{d}))_K + \langle \boldsymbol{d}\times(\boldsymbol{n}\times\boldsymbol{b}), \boldsymbol{u}\rangle_{\partial K}, \tag{3.6a}$$

$$[\boldsymbol{d}\times(\boldsymbol{n}\times\boldsymbol{b})]\cdot\boldsymbol{u} = -[\boldsymbol{n}\times(\boldsymbol{u}\times\boldsymbol{d})]\cdot\boldsymbol{b}. \tag{3.6b}$$

These identities follow from integration by parts and vector product identities.

Next, we multiply (3.2a) through (3.2f) by test functions $(\boldsymbol{G}, \boldsymbol{v}, q, \boldsymbol{J}, \boldsymbol{c}, s)$, integrate by parts all terms, and introduce the numerical flux (3.5) in the boundary terms. This results in a local discrete weak formulation:

$$\mathrm{Re}\,(\boldsymbol{L}_h, \boldsymbol{G})_K + (\boldsymbol{u}_h, \nabla\cdot\boldsymbol{G})_K + \left\langle \hat{\boldsymbol{F}}^1_h\cdot\boldsymbol{n}, \boldsymbol{G}\right\rangle_{\partial K} = 0, \tag{3.7a}$$

$$\begin{aligned}(\boldsymbol{L}_h, \nabla\boldsymbol{v})_K - (p_h, \nabla\cdot\boldsymbol{v})_K - (\boldsymbol{u}_h\otimes\boldsymbol{w}, \nabla\boldsymbol{v})_K \\ +\kappa\,(\boldsymbol{b}_h, \nabla\times(\boldsymbol{v}\times\boldsymbol{d}))_K + \left\langle \hat{\boldsymbol{F}}^2_h\cdot\boldsymbol{n}, \boldsymbol{v}\right\rangle_{\partial K} = (\boldsymbol{g}, \boldsymbol{v})_K,\end{aligned} \tag{3.7b}$$

$$-(\boldsymbol{u}_h, \nabla q)_K + \left\langle \hat{\boldsymbol{F}}^3_h\cdot\boldsymbol{n}, q\right\rangle_{\partial K} = 0, \tag{3.7c}$$

$$\frac{\mathrm{Rm}}{\kappa}(\boldsymbol{J}_h, \boldsymbol{H})_K - (\boldsymbol{b}_h, \nabla\times\boldsymbol{H})_K + \left\langle \hat{\boldsymbol{F}}^4_h\cdot\boldsymbol{n}, \boldsymbol{H}\right\rangle_{\partial K} = 0, \tag{3.7d}$$

$$\begin{aligned}(\boldsymbol{J}_h, \nabla\times\boldsymbol{c})_K - (r_h, \nabla\cdot\boldsymbol{c})_K - \kappa\,(\boldsymbol{u}_h, \boldsymbol{d}\times(\nabla\times\boldsymbol{c}))_K \\ + \left\langle \hat{\boldsymbol{F}}^5_h\cdot\boldsymbol{n}, \boldsymbol{c}\right\rangle_{\partial K} = (\boldsymbol{f}, \boldsymbol{c})_K,\end{aligned} \tag{3.7e}$$

$$-(\boldsymbol{b}_h, \nabla s)_K + \left\langle \hat{\boldsymbol{F}}^6_h\cdot\boldsymbol{n}, s\right\rangle_{\partial K} = 0, \tag{3.7f}$$

for all $(\boldsymbol{G}, \boldsymbol{v}, q, \boldsymbol{H}, \boldsymbol{c}, s) \in \mathbf{G}_h(K)\times\mathbf{V}_h(K)\times\mathbf{Q}_h(K)\times\mathbf{H}_h(K)\times\mathbf{C}_h(K)\times\mathbf{S}_h(K)$ and for all $K\in\Omega_h$, where quantities with subscript h are the discrete counterparts of the continuous ones, for example, $\boldsymbol{u}_h$ and $\boldsymbol{L}_h$ are the discrete approximations of $\boldsymbol{u}$ and $\boldsymbol{L}$.

Since $\hat{\boldsymbol{u}}$, $\hat{p}$, $\hat{\boldsymbol{b}}$, and $\hat{r}$ are facet unknowns introduced in addition to the original unknowns, we need to equip extra equations to make the system (3.7) well-posed. To that end, we observe that an element K communicates with its neighbors only through the trace unknowns. For the E-HDG method to be conservative, we weakly enforce the continuity of the numerical flux (3.5) across each interior edge. Since $\hat{\boldsymbol{u}}_h$ and $\hat{\boldsymbol{b}}_h$ are single-valued on $\mathcal{E}_h$, we automatically have that $[\![\hat{\boldsymbol{F}}_h^1 \cdot \boldsymbol{n}]\!] = \boldsymbol{0}$ and $[\![\hat{\boldsymbol{F}}_h^4 \cdot \boldsymbol{n}]\!] = \boldsymbol{0}$. The conservation constraints to be enforced are reduced to

$$\begin{aligned} \left\langle [\![\hat{\boldsymbol{F}}_h^2 \cdot \boldsymbol{n}]\!], \boldsymbol{\mu} \right\rangle_e = 0, \qquad \left\langle [\![\hat{\boldsymbol{F}}_h^3 \cdot \boldsymbol{n}]\!], \rho \right\rangle_e = 0, \\ \left\langle [\![\hat{\boldsymbol{F}}_h^5 \cdot \boldsymbol{n}]\!], \boldsymbol{\lambda} \right\rangle_e = 0, \qquad \left\langle [\![\hat{\boldsymbol{F}}_h^6 \cdot \boldsymbol{n}]\!], \gamma \right\rangle_e = 0, \end{aligned} \tag{3.8}$$

for all $(\boldsymbol{\mu}, \rho, \boldsymbol{\lambda}, \gamma) \in \mathbf{M}_h(e) \times \mathbf{P}_h(e) \times \boldsymbol{\Lambda}_h(e) \times \boldsymbol{\Gamma}_h(e)$, and for all e in $\mathcal{E}_h^o$. Furthermore, the following constraint on the domain boundary is required in order to establish the well-posedness of our HDG formulations:

$$\langle \hat{\boldsymbol{u}}_h \cdot \boldsymbol{n}, \rho \rangle_e = \langle \boldsymbol{u}_h \cdot \boldsymbol{n}, \rho \rangle_e , \tag{3.9}$$

for all $\rho \in \mathbf{P}_h(e)$ for all e in $\mathcal{E}_h^\partial$. This constraint means that we weakly enforce $\hat{\boldsymbol{u}}_h \cdot \boldsymbol{n} = \boldsymbol{u}_h \cdot \boldsymbol{n}$ on the boundary, and is also used in [66, 84, 86] where hybridized IPDG methods are developed for solving the incompressible Navier-Stokes equations. Finally, we enforce the Dirichlet boundary conditions weakly through the facet unknowns:

$$\langle \hat{\boldsymbol{u}}_h, \boldsymbol{\mu} \rangle_e = \langle \boldsymbol{u}_D, \boldsymbol{\mu} \rangle_e , \qquad \left\langle \hat{\boldsymbol{b}}_h, \boldsymbol{\lambda} \right\rangle_e = \langle \boldsymbol{b}_D, \boldsymbol{\lambda} \rangle_e , \qquad \langle \hat{r}_h, \gamma \rangle_e = 0, \tag{3.10}$$

for all $(\boldsymbol{\mu}, \boldsymbol{\lambda}, \gamma) \in \boldsymbol{M}_h(e) \times \boldsymbol{\Lambda}_h(e) \times \Gamma_h(e)$ for all e in $\mathcal{E}_h^\partial$. In Eq. (3.7)-(3.10) we seek $(\boldsymbol{L}_h, \boldsymbol{u}_h, p_h, \boldsymbol{J}_h, \boldsymbol{b}_h, r_h) \in \mathbf{G}_h \times \mathbf{V}_h \times \mathbf{Q}_h \times \mathbf{H}_h \times \mathbf{C}_h \times \mathbf{S}_h$ and $(\hat{\boldsymbol{u}}_h, \hat{p}, \hat{\boldsymbol{b}}_h, \hat{r}_h) \in \mathbf{M}_h \times \mathbf{P}_h \times \boldsymbol{\Lambda}_h \times \boldsymbol{\Gamma}_h$. For simplicity, we will not state explicitly that equations hold for all test functions, for all elements, or for all edges.

We will refer to $\boldsymbol{L}_h, \boldsymbol{u}_h, p_h, \boldsymbol{J}_h, \boldsymbol{b}_h$, and r_h as the *local variables*, and to equation (3.7) on each element as the *local solver*. This reflects the fact that we can solve for local variables element-by-element as functions of $\hat{\boldsymbol{u}}_h, \hat{p}_h, \hat{\boldsymbol{b}}_h$, and $\hat{r}_h$. On the other hand, we will refer to $\hat{\boldsymbol{u}}_h, \hat{p}_h, \hat{\boldsymbol{b}}_h$, and $\hat{r}_h$ as the *global variables*, which are governed by equations (3.8),(3.10), and (3.9) on the mesh skeleton. For the uniqueness of the discrete pressure p_h, we enforce the discrete counterpart of (3.4):

$$(p_h, 1) = 0. \tag{3.11}$$

3.1. Well-posedness of the E-HDG formulation. In this subsection, we discuss the well-posedness of (3.7)–(3.11). We would like to point out that the result presented in this subsection is also valid for the proposed HDG version in Remark 1.

THEOREM 3.1. *Let Ω be simply connected with one component to $\partial\Omega$. Let α_1, β_1, $\beta_2 \in \mathbb{R}$ such that $\alpha_1 > \frac{1}{2}\|\boldsymbol{w}\|_{L^\infty(\Omega)}$ and $\beta_1 \boldsymbol{T} + \beta_2 \boldsymbol{N} > 0$. The system (3.7)–(3.11) is well-posed, in the sense that given $\boldsymbol{f}$, $\boldsymbol{g}$, $\boldsymbol{u}_D$, and $\boldsymbol{h}_D$, there exists a unique solution $\left(\boldsymbol{L}_h, \boldsymbol{u}_h, p_h, \boldsymbol{J}_h, \boldsymbol{b}_h, r_h, \hat{\boldsymbol{u}}_h, \hat{p}_h, \hat{\boldsymbol{b}}_h, \hat{r}_h\right)$.*

Proof. (3.7)–(3.11) has the same number of equations and unknowns, so it is enough to show that $(\boldsymbol{g}, \boldsymbol{f}, \boldsymbol{u}_D, \boldsymbol{b}_D) = \boldsymbol{0}$ implies $(\boldsymbol{L}_h, \boldsymbol{u}_h, p_h, \boldsymbol{J}_h, \boldsymbol{b}_h, r_h, \hat{\boldsymbol{u}}_h, \hat{p}_h, \hat{\boldsymbol{b}}_h, \hat{r}_h) = \boldsymbol{0}$. To begin, we take $(\boldsymbol{G}, \boldsymbol{v}, q, \boldsymbol{J}, \boldsymbol{c}, s) = (\boldsymbol{L}_h, \boldsymbol{u}_h, p_h, \boldsymbol{J}_h, \boldsymbol{b}_h, r_h)$, integrate by parts the first four terms of (3.7b) and the first term of (3.7e), sum the resulting equations in

(3.7), and sum over all elements to arrive at

$$\begin{aligned}
&\mathrm{Re}\,\|\boldsymbol{L}_h\|_0^2+\frac{\mathrm{Rm}}{\kappa}\|\boldsymbol{J}_h\|_0^2-\langle\hat{\boldsymbol{u}}_h\otimes\boldsymbol{n},\boldsymbol{L}_h\rangle+\left\langle\frac{m}{2}\boldsymbol{u}_h,\boldsymbol{u}_h\right\rangle+\langle\alpha_1(\boldsymbol{u}_h-\hat{\boldsymbol{u}}_h),\boldsymbol{u}_h\rangle\\
&+\langle\hat{p}_h\boldsymbol{n},\boldsymbol{u}_h\rangle+\left\langle\frac{1}{2}\kappa\boldsymbol{d}\times\left(\boldsymbol{n}\times\hat{\boldsymbol{b}}_h\right),\boldsymbol{u}_h\right\rangle-\left\langle\boldsymbol{n}\times\hat{\boldsymbol{b}}_h,\boldsymbol{J}_h\right\rangle+\langle\hat{r}_h\boldsymbol{n},\boldsymbol{b}_h\rangle\\
&+\left\langle\left(\beta_1\boldsymbol{T}+\beta_2\boldsymbol{N}\right)(\boldsymbol{b}_h-\hat{\boldsymbol{b}}_h),\boldsymbol{b}_h\right\rangle-\left\langle\frac{1}{2}\kappa\boldsymbol{n}\times(\hat{\boldsymbol{u}}_h\times\boldsymbol{d}),\boldsymbol{b}_h\right\rangle=0,
\end{aligned}\tag{3.12}$$

where we have used $\nabla\cdot\boldsymbol{w}=0$ and the following integration by parts identities:

$$-(\boldsymbol{u}_h,\boldsymbol{w}\cdot\nabla\boldsymbol{u}_h)_K=-\frac{1}{2}(\boldsymbol{w},\nabla(\boldsymbol{u}_h\cdot\boldsymbol{u}_h))_K=-\left\langle\frac{m}{2}\boldsymbol{u}_h,\boldsymbol{u}_h\right\rangle_{\partial K}.$$

Next, setting $(\boldsymbol{\mu},\rho,\boldsymbol{\lambda},\gamma)=(\hat{\boldsymbol{u}}_h,\hat{p}_h,\hat{\boldsymbol{b}}_h,\hat{r}_h)$, and summing (3.8) over all interior edges give

$$\begin{aligned}
&\left\langle-\boldsymbol{L}_h\boldsymbol{n}+m\boldsymbol{u}_h+\hat{p}_h\boldsymbol{n}+\frac{1}{2}\kappa\boldsymbol{d}\times(\boldsymbol{n}\times\boldsymbol{b}_h)+\alpha_1\left(\boldsymbol{u}_h-\hat{\boldsymbol{u}}_h\right),\hat{\boldsymbol{u}}_h\right\rangle_{\partial\Omega_h\setminus\partial\Omega}\\
&\qquad+\langle\boldsymbol{u}_h\cdot\boldsymbol{n},\hat{p}_h\rangle_{\partial\Omega_h\setminus\partial\Omega}\\
&+\left\langle\boldsymbol{n}\times\boldsymbol{J}_h+\hat{r}_h\boldsymbol{n}-\frac{1}{2}\kappa\boldsymbol{n}\times(\boldsymbol{u}_h\times\boldsymbol{d})+(\beta_1\boldsymbol{T}+\beta_2\boldsymbol{N})\left(\boldsymbol{b}_h-\hat{\boldsymbol{b}}_h\right),\hat{\boldsymbol{b}}_h\right\rangle_{\partial\Omega_h\setminus\partial\Omega}\\
&\qquad+\langle\boldsymbol{b}_h\cdot\boldsymbol{n},\hat{r}_h\rangle_{\partial\Omega_h\setminus\partial\Omega}=0,
\end{aligned}\tag{3.13}$$

where we used the continuity of $\boldsymbol{d}$ and the single-valued nature across the element boundaries of global variables to eliminate $\langle\boldsymbol{d}\times(\boldsymbol{n}\times\hat{\boldsymbol{b}}_h),\hat{\boldsymbol{u}}_h\rangle_{\partial\Omega_h\setminus\partial\Omega}$ and $\langle\boldsymbol{n}\times(\hat{\boldsymbol{u}}_h\times\boldsymbol{d}),\hat{\boldsymbol{b}}_h\rangle_{\partial\Omega_h\setminus\partial\Omega}$.

Since $\boldsymbol{u}_D=\boldsymbol{0}$ and $\boldsymbol{b}_D=\boldsymbol{0}$ by assumption, we conclude from the boundary conditions (3.10) that $\hat{\boldsymbol{u}}_h=\boldsymbol{0}$, $\hat{\boldsymbol{b}}_h=\boldsymbol{0}$, and $\hat{r}_h=0$ on $\partial\Omega$. In addition, from the constraint (3.9) we also have $\langle\boldsymbol{u}_h\cdot\boldsymbol{n},\hat{p}_h\rangle_e=\langle\hat{\boldsymbol{u}}_h\cdot\boldsymbol{n},\hat{p}_h\rangle_e$ on the boundary and hence $\langle\boldsymbol{u}_h\cdot\boldsymbol{n},\hat{p}_h\rangle_{\partial\Omega}=0$. Subtracting (3.13) from (3.12) and using the fact that $\hat{\boldsymbol{u}}_h,\hat{\boldsymbol{b}}_h,\hat{r}_h$, and $\langle\boldsymbol{u}_h\cdot\boldsymbol{n},\hat{p}_h\rangle_{\partial\Omega}$ vanish on the physical boundary $\partial\Omega$, we arrive at

$$\begin{aligned}
&\mathrm{Re}\,\|\boldsymbol{L}_h\|_0^2+\frac{\mathrm{Rm}}{\kappa}\|\boldsymbol{J}_h\|_0^2+\langle\alpha_1(\boldsymbol{u}_h-\hat{\boldsymbol{u}}_h),(\boldsymbol{u}_h-\hat{\boldsymbol{u}}_h)\rangle+\left\langle\frac{m}{2}\boldsymbol{u}_h,\boldsymbol{u}_h\right\rangle\\
&-\langle m\boldsymbol{u}_h,\hat{\boldsymbol{u}}_h\rangle+\left\langle(\beta_1\boldsymbol{T}+\beta_2\boldsymbol{N})\left(\boldsymbol{b}_h-\hat{\boldsymbol{b}}_h\right),\boldsymbol{b}_h-\hat{\boldsymbol{b}}_h\right\rangle=0.
\end{aligned}\tag{3.14}$$

Finally, using the fact that $\boldsymbol{w}\in H(div,\Omega)$ and $\hat{\boldsymbol{u}}_h=\boldsymbol{0}$ on $\partial\Omega$, we can freely add $0=\left\langle\frac{m}{2}\hat{\boldsymbol{u}}_h,\hat{\boldsymbol{u}}_h\right\rangle$ to rewrite (3.14) as

$$\begin{aligned}
&\mathrm{Re}\,\|\boldsymbol{L}_h\|_0^2+\frac{\mathrm{Rm}}{\kappa}\|\boldsymbol{J}_h\|_0^2+\left\langle\left(\alpha_1+\frac{m}{2}\right)(\boldsymbol{u}_h-\hat{\boldsymbol{u}}_h),(\boldsymbol{u}_h-\hat{\boldsymbol{u}}_h)\right\rangle\\
&+\left\langle(\beta_1\boldsymbol{T}+\beta_2\boldsymbol{N})\left(\boldsymbol{b}_h-\hat{\boldsymbol{b}}_h\right),\boldsymbol{b}_h-\hat{\boldsymbol{b}}_h\right\rangle=0.
\end{aligned}\tag{3.15}$$

Recalling $\alpha_1>\frac{1}{2}\|\boldsymbol{w}\|_{L^\infty}$ and $\beta_1\boldsymbol{T}+\beta_2\boldsymbol{N}>0$, we can conclude that $\boldsymbol{L}_h=\boldsymbol{0}$, $\boldsymbol{J}_h=\boldsymbol{0}$, that $\boldsymbol{u}_h=\hat{\boldsymbol{u}}_h$, and $\boldsymbol{b}_h=\hat{\boldsymbol{b}}_h$ on $\mathcal{E}_h$.

Now, we integrate (3.7a) by parts to obtain $\nabla\boldsymbol{u}_h=\boldsymbol{0}$ in K, which implies that $\boldsymbol{u}_h$ is element-wise constant. The fact that $\boldsymbol{u}_h=\hat{\boldsymbol{u}}_h$ on $\mathcal{E}_h$ means $\boldsymbol{u}_h$ is continuous across $\mathcal{E}_h$. Since $\boldsymbol{u}_h=\boldsymbol{0}$ on $\partial\Omega$, we conclude that $\boldsymbol{u}_h=\boldsymbol{0}$ and therefore $\hat{\boldsymbol{u}}_h=\boldsymbol{0}$.

Since $\boldsymbol{b}_h = \hat{\boldsymbol{b}}_h$ on $\mathcal{E}_h$, $\boldsymbol{b}_h$ is continuous on Ω. Integrating both (3.7d) and (3.7f) by parts, we have $\nabla \times \boldsymbol{b}_h = \boldsymbol{0}$ and $\nabla \cdot \boldsymbol{b}_h = 0$ on Ω. When $\boldsymbol{b}_h \in H(div, \Omega) \cap H(curl, \Omega)$ and $\boldsymbol{b}_h = \boldsymbol{0}$ on $\partial\Omega$, and recalling that Ω is simply connected with one component to the boundary, there is a constant $C > 0$ such that $\|\boldsymbol{b}_h\|_0 \leq C(\|\nabla \cdot \boldsymbol{b}_h\|_0 + \|\nabla \times \boldsymbol{b}_h\|_0)$ [46, Lemma 3.4]. This implies that $\boldsymbol{b}_h = \boldsymbol{0}$, and hence $\hat{\boldsymbol{b}}_h = \boldsymbol{0}$.

Taking account of the vanishing variables we had discussed, integrating by parts reduces (3.7b) and (3.7e) to:

$$(\nabla p_h, \boldsymbol{v})_K - \langle (p_h - \hat{p}_h)\, \boldsymbol{n}, \boldsymbol{v} \rangle_{\partial K} = 0, \tag{3.16}$$

and

$$(\nabla r_h, \boldsymbol{c})_K - \langle (r_h - \hat{r}_h)\, \boldsymbol{n}, \boldsymbol{c} \rangle_{\partial K} = 0, \tag{3.17}$$

respectively. Given that $p_h|_K$, $r_h|_K \in \mathcal{P}_{k-1}(K)$ and a simplicial mesh is used, we can invoke the argument of Nédélec space to conclude that $p_h = \hat{p}_h$ and $r_h = \hat{r}_h$ on ∂K (Proposition 4.6 in [85]). This implies that $(\nabla p_h, \boldsymbol{v})_K = 0$ and $(\nabla r_h, \boldsymbol{c})_K = 0$. Thus, p_h and r_h are elementwise constants. Since $r_h = \hat{r}_h$ on $\mathcal{E}_h^o$, then r_h is continuous on Ω, and since $r_h = 0$ on $\partial\Omega$, we can conclude that $r_h = 0$, and hence $\hat{r}_h = 0$. Finally, we use the result $p_h = \hat{p}_h$ on $\mathcal{E}_h^o$ to conclude that p_h is continuous and a constant on Ω. Using the zero-average condition (3.11) yields $p_h = 0$ and hence $\hat{p}_h = 0$. ∎

3.2. Well-posedness of the local solver. A key advantage of HDG or E-HDG methods is the decoupling computation of the local variables $(\boldsymbol{L}_h, \boldsymbol{u}_h, p_h, \boldsymbol{J}_h, \boldsymbol{b}_h, r_h)$ and the global variables $(\hat{\boldsymbol{u}}_h, \hat{p}_h, \hat{\boldsymbol{b}}_h, \hat{r}_h)$. In our E-HDG scheme, we first solve (3.7) for local unknowns $(\boldsymbol{L}_h, \boldsymbol{u}_h, p_h, \boldsymbol{J}_h, \boldsymbol{b}_h, r_h)$ as a function of $(\hat{\boldsymbol{u}}_h, \hat{p}_h, \hat{\boldsymbol{b}}_h, \hat{r}_h)$ (local solver), then these are substituted into (3.8) on the mesh skeleton to solve for the unknowns $(\hat{\boldsymbol{u}}_h, \hat{p}_h, \hat{\boldsymbol{b}}_h, \hat{r}_h)$ (global solver). Finally, $(\boldsymbol{L}_h, \boldsymbol{u}_h, p_h, \boldsymbol{J}_h, \boldsymbol{b}_h, r_h)$ are computed with the local solver using $(\hat{\boldsymbol{u}}_h, \hat{p}_h, \hat{\boldsymbol{b}}_h, \hat{r}_h)$, so well-posedness of the local solver is essential. It should be emphasized again that the result presented in this subsection is also valid for the HDG version in Remark 1.

THEOREM 3.2. *Let $\alpha_1, \beta_1, \beta_2 \in \mathbb{R}$ such that $\alpha_1 > \frac{1}{2}\|\boldsymbol{w}\|_{L^\infty(\Omega)}$ and $\beta_1 \boldsymbol{T} + \beta_2 \boldsymbol{N} > 0$. The local solver given by (3.7) is well-posed. In other words, given $(\hat{\boldsymbol{u}}_h, \hat{p}_h, \hat{\boldsymbol{b}}_h, \hat{r}_h, \boldsymbol{g}, \boldsymbol{f}, \rho_h)$, there exists a unique solution $(\boldsymbol{L}_h, \boldsymbol{u}_h, p_h, \boldsymbol{J}_h, \boldsymbol{b}_h, r_h)$ of the system.*

Proof. We show that $(\hat{\boldsymbol{u}}_h, \hat{p}_h, \hat{\boldsymbol{b}}_h, \hat{r}_h, \boldsymbol{g}, \boldsymbol{f}, \rho_h) = \boldsymbol{0}$ implies $(\boldsymbol{L}_h, \boldsymbol{u}_h, p_h, \boldsymbol{J}_h, \boldsymbol{b}_h, r_h) = \boldsymbol{0}$. To begin, set $(\hat{\boldsymbol{u}}_h, \hat{p}_h, \hat{\boldsymbol{b}}_h, \hat{r}_h, \boldsymbol{g}, \boldsymbol{f}, \rho_h) = \boldsymbol{0}$. Take $(\boldsymbol{G}, \boldsymbol{v}, q, \boldsymbol{J}, \boldsymbol{c}, s) = (\boldsymbol{L}_h, \boldsymbol{u}_h, p_h, \boldsymbol{J}_h, \boldsymbol{b}_h, r_h)$, integrate by parts the first four terms in (3.7b) and the first term in (3.7e), and sum the resulting equations to get

$$\begin{aligned} &\operatorname{Re}\|\boldsymbol{L}_h\|_{0,K}^2 + \left\langle \left(\alpha_1 + \frac{m}{2}\right) \boldsymbol{u}_h, \boldsymbol{u}_h \right\rangle_{\partial K} \\ &\quad + \frac{\mathrm{Rm}}{\kappa}\|\boldsymbol{J}_h\|_{0,K}^2 + \langle (\beta_1 \boldsymbol{T} + \beta_2 \boldsymbol{N})\, \boldsymbol{b}_h, \boldsymbol{b}_h \rangle_{\partial K} = 0. \end{aligned} \tag{3.18}$$

Recalling $\alpha_1 > \frac{1}{2}\|\boldsymbol{w}\|_{L^\infty}$ and $\beta_1 \boldsymbol{T} + \beta_2 \boldsymbol{N} > 0$, we can yield

$$\boldsymbol{L}_h = \boldsymbol{0}, \quad \boldsymbol{J}_h = \boldsymbol{0}, \quad \text{in } K; \qquad \boldsymbol{u}_h = \boldsymbol{0}, \quad \boldsymbol{b}_h = \boldsymbol{0}, \quad \text{on } \partial K.$$

Using an argument similar to that in Section 3.1 we can conclude $\boldsymbol{u}_h = \boldsymbol{b}_h = \boldsymbol{0}$ in K. From (3.7b) and (3.7e), we have:

$$-(p_h, \nabla \cdot \boldsymbol{v})_K = 0, \quad \forall \boldsymbol{v} \in \mathbf{V}_h(K), \tag{3.19}$$

and

$$-\left(r_h, \nabla\cdot\boldsymbol{c}\right)_K = 0, \quad \forall \boldsymbol{c}\in\mathbf{C}_h\left(K\right), \tag{3.20}$$

respectively. Since the space $\{q : q = \nabla\cdot\boldsymbol{v}, \forall\boldsymbol{v}\in\mathbf{V}_h\left(K\right)\} \supseteq \mathbf{Q}_h\left(K\right)$ and $\{s : s = \nabla\cdot\boldsymbol{c}, \forall\boldsymbol{c}\in\mathbf{C}_h\left(K\right)\} \supseteq \mathbf{S}_h\left(K\right)$, we can pick $\nabla\cdot\boldsymbol{v} = p_h$ and $\nabla\cdot\boldsymbol{c} = r_h$ and conclude that $p_h = r_h = 0$ in K. ∎

3.3. Conservation properties of the E-HDG method. In this section, we prove that our method is divergence-free and $H\left(div\right)$-conforming for both velocity (i.e., the exactness of mass conservation) and magnetic (i.e., the absence of magnetic monopoles) fields. Same conclusions can be drawn for the HDG version in Remark 1. It is worth mentioning that in this work a simplicial mesh is assumed to be used. In fact, the proofs of propositions presented in this section are only valid for a straight-sided mesh.

PROPOSITION 1 (divergence-free property and $H\left(div\right)$-conformity for the velocity field). *Let $\boldsymbol{u}_h\in\mathbf{V}_h$ and $\hat{\boldsymbol{u}}_h\in\mathbf{M}_h$ be the solution to the proposed E-HDG discretization (3.7)-(3.11), then*

$$\nabla\cdot\left(\boldsymbol{u}_h|_K\right) = 0, \qquad \forall K\in\Omega_h; \tag{3.21a}$$

$$[\![\boldsymbol{u}_h\cdot\boldsymbol{n}]\!]|_e = 0, \qquad \forall e\in\mathcal{E}_h^o. \tag{3.21b}$$

$$\boldsymbol{u}_h\cdot\boldsymbol{n} = \hat{\boldsymbol{u}}_h\cdot\boldsymbol{n}, \qquad \text{on } e \text{ and } \forall e\in\mathcal{E}_h^\partial. \tag{3.21c}$$

Proof. Apply integration-by-parts to Eq. (3.7c):

$$\left(\nabla\cdot\left(\boldsymbol{u}_h|_K\right), q\right)_K = 0, \quad \forall q\in\mathbf{Q}_h(K), \forall K\in\Omega_h. \tag{3.22}$$

Since $\nabla\cdot\left(\boldsymbol{u}_h|_K\right)\in\mathbf{Q}_h(K)$, we can take $q = \nabla\cdot\left(\boldsymbol{u}_h|_K\right)$, yielding $\|\nabla\cdot\left(\boldsymbol{u}_h|_K\right)\|_{0,K}^2 = 0$, which implies that $\nabla\cdot\left(\boldsymbol{u}_h|_K\right) = 0$ for all $K\in\Omega_h$. It follows from Eq. (3.8) that:

$$\left\langle [\![\hat{\boldsymbol{F}}_h^3\cdot\boldsymbol{n}]\!], \rho\right\rangle_e = \langle [\![\boldsymbol{u}_h\cdot\boldsymbol{n}]\!], \rho\rangle_e = 0, \quad \forall\rho\in\mathbf{P}_h(e), \forall e\in\mathcal{E}_h^o. \tag{3.23}$$

Since $[\![\boldsymbol{u}_h\cdot\boldsymbol{n}]\!]|_e\in\mathbf{P}_h(e)$[3], we can take $\rho = [\![\boldsymbol{u}_h\cdot\boldsymbol{n}]\!]$, yielding $\|[\![\boldsymbol{u}_h\cdot\boldsymbol{n}]\!]\|_{0,e}^2 = 0$ for all $e\in\mathcal{E}_h^o$. Thus, $[\![\boldsymbol{u}_h\cdot\boldsymbol{n}]\!]|_e = 0$ for all $e\in\mathcal{E}_h^o$. The proof of Eq. (3.21c) follows the same argument with the aid of Eq. (3.9). ∎

PROPOSITION 2 (divergence-free property and $H\left(div\right)$-conformity for the magnetic field). *Let $\boldsymbol{b}_h\in\mathbf{C}_h$ and $\hat{\boldsymbol{b}}_h\in\boldsymbol{\Lambda}_h$ be the solution to the proposed E-HDG discretization (3.7)-(3.11), then*

$$\nabla\cdot\left(\boldsymbol{b}_h|_K\right) = 0, \qquad \forall K\in\Omega_h; \tag{3.24a}$$

$$[\![\boldsymbol{b}_h\cdot\boldsymbol{n}]\!]|_e = 0, \qquad \forall e\in\mathcal{E}_h^o. \tag{3.24b}$$

Proof. The result holds by directly following the similar argument as the proof of Proposition 1. ∎

REMARK 2. *As can be seen, both Propositions 1 and 2 also hold true for the nonlinear case. That is, they are still valid if $\boldsymbol{w}$ and $\boldsymbol{d}$ are replaced by $\boldsymbol{u}_h$ and $\boldsymbol{b}_h$ in (3.7)-(3.8).*

[3]Note that the statement $[\![\boldsymbol{u}_h\cdot\boldsymbol{n}]\!]|_e\in\mathbf{P}_h(e)$ do not hold for a curve mesh since $\boldsymbol{n}$ is not constant anymore.

4. Numerical Results. A nonlinear solver can be constructed through the employment of the linear E-HDG (or HDG in Remark 1) scheme given by (3.7)-(3.11) in a Picard iteration. If we consider the linearized MHD equations (3.1) to be a linear map $(\boldsymbol{w}, \boldsymbol{d}) \mapsto (\boldsymbol{u}, \boldsymbol{b})$, then any fixed point of that mapping is a solution to the nonlinear incompressible viso-resistive MHD equations (1.1). With this in mind, we can use the general linearized incompressible MHD E-HDG scheme (3.7)–(3.11) in an iterative manner to numerically solve the nonlinear incompressible MHD equations. The convergence of such an interaction is investigated in [77]. Let the superscript denote an iteration number, we set the initial guess $\boldsymbol{u}_h^0 = \boldsymbol{0}$ and $\boldsymbol{b}_h^0 = \boldsymbol{0}$ and the stopping criterion

$$TOL := \max\left\{ \frac{\left\|\boldsymbol{u}_h^i - \boldsymbol{u}_h^{i-1}\right\|_0}{\left\|\boldsymbol{u}_h^i\right\|_0}, \frac{\left\|\boldsymbol{b}_h^i - \boldsymbol{b}_h^{i-1}\right\|_0}{\left\|\boldsymbol{b}_h^i\right\|_0} \right\} < \varepsilon, \tag{4.1}$$

where ε is a user-defined tolerance. In particular, we take $\varepsilon = O(10^{-10})$ in all numerical experiments for the nonlinear examples.

In this section, a series of numerical experiments is presented to illustrate the capability of the E-HDG method in both linear and nonlinear scenarios. First, a comparison is drawn between the proposed HDG and E-HDG methods regarding the DOFs and the actual computational time (wall-clock time). Then the order of accuracy for the linear scheme is numerically investigated by applying the E-HDG method to two- and three-dimensional problems with smooth solutions. The convergence of a two-dimensional singular problem, defined on a nonconvex domain, is also presented. Moreover, the pressure-robustness of our method is numerically demonstrated by perturbing smooth manufactured solutions. Finally, the order of accuracy for the nonlinear solver, where the linear scheme is integrated into a Picard iteration, is studied through two- and three-dimensional problems featuring smooth solutions, including a stationary liquid duct flow in plasma physics and manufactured solutions. It should be emphasized that the divergence-free property and $H(div)$-conformity still obviously hold for our nonlinear solver and will be validated through numerical demonstrations.

Our methods—both HDG and E-HDG)—are implemented based on the Modular Finite Element Method (MFEM) library [4]. Furthermore, we use the direct solver of MUMPS [2, 3] through PETSc [10, 9] to solve the systems of linear equations composed by the Schur complement (or static condensation) resulting from the discretization (3.7)–(3.11). In addition, we take stabilization parameters $\alpha_1 \in \{125, 1000\}$ and $\beta_1 = \beta_2 \in \{1, 100, 1000\}$. Although it is proved that the well-posedness of both local and global solvers can be guaranteed by the conditions $\alpha_1 > \frac{1}{2}\|\boldsymbol{w}\|_{L^\infty}$, and $\beta_1 \boldsymbol{T} + \beta_2 \boldsymbol{N} > 0$, we numerically found that small increments in the values of the stabilization parameters can improve the order of accuracy. However, large values (i.e., $O(10^4)$ or larger) of the parameters can cause serious adverse effects in convergence. It could be caused by the increased stiffness (condition number).

REMARK 3. *In all numerical experiments, the physical parameters are given and comparisons of different values of the parameters are made in some cases to provide an insight into how robust our method is. Although our well-posedness analysis shows the stability of our methods regardless of what values of Re, Rm, and κ are, the solver will still be affected by these parameters which characterize the condition number of the linear system. It is worth emphasizing that the linear system to be solved is already near singular owing to the pressure variable (See Remark 5). Thus, it could be expected that the higher these values are, the harder the problem to be solved.*

REMARK 4. *In this work, the auxiliary variables* $\boldsymbol{L}_h$ *and* $\boldsymbol{J}_h$ *can be locally eliminated through local Eq.* (3.7a) *and* (3.7d)*, respectively. Since the numerical flux defined in* (3.7a) *only associates with a single global variable* $\hat{\boldsymbol{u}}_h$*, the local variable* $\boldsymbol{L}_h$ *can be expressed by* $\boldsymbol{u}_h$ *and* $\hat{\boldsymbol{u}}_h$*, thanks to the block diagonal structure endowed by the term* $\mathrm{Re}\,(\boldsymbol{L}_h, \boldsymbol{G})_K$*. A similar procedure can also be followed to express* $\boldsymbol{J}_h$ *by* $\boldsymbol{b}_h$ *and* $\hat{\boldsymbol{b}}_h$ *with the help of Eq.* (3.7d)*. Through the elimination, the assembly operation (construct the local Schur complement and allocate it to the global matrix) and reconstruction operation (solve for the local variables with the given global variables) can be computationally cheaper.*

REMARK 5. *Even though the well-posedness of the method is proved in Theorem 3.1, the inclusion of the pressure constraint given in* (3.11) *is not straightforward to implement. Note that the discretization is ill-posed without the pressure constraint, and the local variable* p_h *and global variable* $\hat{p}_h$ *can only be determined up to a constant. Such a singular system can still be handled by a Krylov type of iterative solver without encountering breakdowns [15, 36]. However, in order to use a direct solver, an additional treatment is necessary. In this paper, we restrict one DOF of the global variable* $\hat{p}_h$ *to be zero such that both* p_h *and* $\hat{p}_h$ *can be determined. Once the system is solved by the direct solver, we then enforce the pressure constraint* (3.11) *by post-processing.*

REMARK 6. *All* L^∞*-norms are computed as the maximum norm of the function values evaluated on all elements using a set of quadrature points with the order of accuracy* $2k + 3$*.*

4.1. Computational Performance of the proposed HDG and E-HDG methods. In this subsection, we discuss the computational costs of the HDG and the E-HDG methods in which the discretization is based on (3.7)-(3.11) but with different trace approximation spaces (see Remark 1). Table 4.1 summarizes the DOFs needed by the HDG and E-HDG methods, and Table 4.2 summarizes the corresponding computational time. The values presented in each cell of Table 4.2 denote the total wall-clock time spent by the entire process. This includes the three main tasks: the assembly (locally constructing the Schur complement and allocating it to the global matrix), the solution of the system of equations (obtaining the global variables), and the local reconstruction (recovering the local variables from the given global variables through the solution of the local equations (3.7)). The measurements are based on the average of five runs, with each run recording the maximal time among all MPI processes.

The reduction in DOFs becomes notably more pronounced for three-dimensional cases, particularly on finer meshes. For example, applying the E-HDG method with $k = 1$ on a mesh comprising 24576 elements results in a maximum DOF reduction of up to 72.58%. This reduction is directly reflected in the computational time, see Table 4.2, where a 47.74% saving in total computational time is achieved. The efficiency of the E-HDG method is further illustrated in Figure 4.1 by comparing its accuracy and computational time with the HDG method for $k = 1, 2$[4] in the context of three-dimensional cases. However, on coarser meshes, despite substantial reductions in DOFs, the corresponding savings in computational time are limited (perhaps due to the efficiency of MUMPS [2, 3]). This discrepancy can be explained through Table

[4]The $k = 3, 4$ is not included since both approaches have similar efficiency if the mesh consisting of 3072 elements is used. In addition, the HDG method is not applicable with the MUMPS solver when the mesh is refined further owing to insufficient memory.

4.3 and Table 4.4. The former delineates the wall-clock time spent by the linear solver, while the latter encapsulates the times allocated to the assembly and the local reconstruction tasks. Analysis of Table 4.4 reveals that the times devoted to assembly and local reconstruction remain similar for both methods irrespective of mesh refinement, approximation degree, or dimension. On the other hand, the reduction trend in total computational time presented in Table 4.2 aligns closely with the computational time required by the linear solver detailed in Table 4.3. This alignment suggests that the advantage of downsizing DOFs may become more substantial when the linear solver time dominates the overall computational time. In essence, while reducing DOFs may not significantly impact the assembly and reconstruction times for the HDG and E-HDG methods, it notably enhances the efficiency of the linear solver in the E-HDG method for larger problems.

In addition to the reduction on computational time, reducing DOFs also adds advantages in memory management and this can be seen in Table 4.2. On the three-dimensional mesh consisting of 24576 elements, the linear solver fails when using the HDG methods along with $k = 3$ and $k = 4$ due to insufficient memory[5]. In contrast, such challenges can be overcome by using the E-HDG method, where the linear solver remains operational under identical circumstances.

Two-dimensions

DOFs used in the HDG method

elem. #	$k=1$	$k=2$	$k=3$	$k=4$
2	60	90	120	150
8	192	288	384	480
32	672	1.01E+03	1.34E+03	1.68E+03
128	2.50E+03	3.74E+03	4.99E+03	6.24E+03
512	9.60E+03	1.44E+04	1.92E+04	2.40E+04

DOFs used in the E-HDG method

elem. #	$k=1$	$k=2$	$k=3$	$k=4$
2	36	66	96	126
8	100	196	292	388
32	324	660	996	1.33E+03
128	1.16E+03	2.40E+03	3.65E+03	4.90E+03
512	4.36E+03	9.16E+03	1.40E+04	1.88E+04

Percentage of reduction in DOFs (%)

elem. #	$k=1$	$k=2$	$k=3$	$k=4$
2	-40.00	-26.67	-20.00	-16.00
8	-47.92	-31.94	-23.96	-19.17
32	-51.79	-34.52	-25.89	-20.71
128	-53.69	-35.79	-26.84	-21.47
512	- 54.62	-36.42	-27.31	-21.85

Three-dimensions

DOFs used in the HDG method

elem. #	$k=1$	$k=2$	$k=3$	$k=4$
6	432	864	1.44E+03	2.16E+03
48	2.88E+03	5.76E+03	9.60E+03	1.44E+04
364	2.07E+04	4.15E+04	6.91E+04	1.04E+05
3072	1.57E+05	3.13E+05	5.22E+05	7.83E+05
24576	**1.22E+06**	2.43E+06	4.06E+06	6.08E+06

DOFs used in the E-HDG method

elem. #	$k=1$	$k=2$	$k=3$	$k=4$
6	156	378	744	1.25E+03
48	882	2.19E+03	4.46E+03	7.69E+03
364	5.93E+03	1.47E+04	3.05E+04	5.31E+04
3072	4.35E+04	1.08E+05	2.24E+05	3.93E+05
24576	**3.34E+05**	8.24E+05	1.72E+06	3.02E+06

Percentage of reduction in DOFs (%)

elem. #	$k=1$	$k=2$	$k=3$	$k=4$
6	-63.89	-56.25	-48.33	-41.94
48	-69.38	-61.98	-53.56	-46.62
364	-71.38	-64.45	-55.93	-48.79
3072	-72.21	-65.59	-57.05	-49.83
24576	**-72.58**	-66.14	-57.59	-50.33

Table 4.1: The summary of DOFs used in E-HDG and HDG discretizations given by (3.7)-(3.11). Note that k denotes the degree of approximation and "elem. #" indicates the number of elements used in a given mesh.

4.2. Linear examples. A series of linear numerical experiments is carried out to verify our method in this subsection. We first analyze the accuracy and the convergence in two dimensions for the case of a smooth manufactured solution. In addition, the pressure robustness of our method is also tested. We then analyze the accuracy and convergence for a singular manufactured solution. Finally, we perform the analysis of the accuracy, convergence, and pressure robustness for a smooth manufactured

[5]Such breakdown can be avoided by using an iterative solver. However, the design of a preconditioned iterative solver is beyond the scope of this paper, and hence we will pursue this in our future work (see also our previous work in [77]).

Two-dimensions

Total number of MPI processes

elem. #	$k=1$	$k=2$	$k=3$	$k=4$
2	1	1	1	1
8	1	1	1	1
32	2	2	2	2
128	2	2	2	2
512	4	4	4	4

Total wall-clock time by the HDG method (sec)

elem. #	$k=1$	$k=2$	$k=3$	$k=4$
2	0.02	0.03	0.07	0.18
8	0.03	0.09	0.25	0.69
32	0.05	0.18	0.50	1.39
128	0.15	0.67	1.98	5.54
512	0.31	1.39	4.01	11.29

Total wall-clock time by the E-HDG method (sec)

elem. #	$k=1$	$k=2$	$k=3$	$k=4$
2	0.01	0.03	0.07	0.18
8	0.02	0.09	0.25	0.69
32	0.05	0.18	0.50	1.39
128	0.14	0.66	1.96	5.51
512	0.27	1.36	3.98	11.21

Reduction in total computational time (%)

elem. #	$k=1$	$k=2$	$k=3$	$k=4$
2	-50.00	0.00	0.00	0.00
8	-33.33	0.00	0.00	0.00
32	0.00	0.00	0.00	0.00
128	-6.67	-1.49	-1.01	-0.54
512	-12.90	-2.16	-0.75	-0.71

Three-dimensions

Total number of MPI processes

elem. #	$k=1$	$k=2$	$k=3$	$k=4$
6	1	1	1	2
48	1	2	2	2
364	2	4	4	8
3072	2	8	8	16
24576	**4**	16	16	32

Total wall-clock time by the HDG method (sec)

elem. #	$k=1$	$k=2$	$k=3$	$k=4$
6	0.17	1.81	11.06	25.04
48	1.17	7.04	44.79	197.09
364	4.96	29.47	182.88	412.77
3072	43.90	127.43	783.20	1726.52
24576	**303.48**	879.87	-	-

Total wall-clock time by the E-HDG method (sec)

elem. #	$k=1$	$k=2$	$k=3$	$k=4$
6	0.16	1.77	11.03	25.05
48	1.14	6.93	45.03	198.85
364	4.65	28.49	182.44	404.38
3072	37.91	117.19	739.76	1650.05
24576	**158.59**	522.89	3341.03	7473.77

Reduction in total computational time (%)

elem. #	$k=1$	$k=2$	$k=3$	$k=4$
6	-5.88	-2.21	-0.27	0.04
48	-2.56	-1.56	0.54	0.89
364	-6.25	-3.33	-0.24	-2.03
3072	-13.64	-8.04	-5.55	-4.43
24576	**-47.74**	-40.57	-	-

Table 4.2: The summary of total computational time (the averaged maximum of wall-clock time over five runs of identical setting, among all MPI processes) taken by E-HDG and HDG methods to solve two- and three-dimensional problems with the discretization given in (3.7)-(3.11). The two-dimensional problem is the one presented in Section 4.2.1 with $\mathrm{Re} = \mathrm{Rm} = 1$ and the three-dimensional problem is the one presented in Section 4.2.3 with $\mathrm{Re} = \mathrm{Rm} = 1$. Note that k denotes the degree of approximation and "elem. #" indicates the number of elements used in a given mesh.

solution in three dimensions.

4.2.1. Two-dimensional smooth manufactured solution. This example illustrates the convergence of the E-HDG scheme applied to a problem posed on the square domain $\Omega = (0,1) \times (0,1)$. In particular, the two-dimensional manufactured vortex solution considered in [47] is adopted. We take $\mathrm{Re} = \mathrm{Rm} \in \{1, 1000\}$ and $\kappa = 1$, and set $\boldsymbol{g}$ and $\boldsymbol{f}$ such that the manufactured solution for (3.2)-(3.4) is

$$\boldsymbol{u} = \begin{pmatrix} -2x^2e^x\left(-y^2+y\right)(2y-1)(x-1)^2, \\ -xy^2e^x\left(x(x+3)-2\right)(x-1)(y-1)^2 \end{pmatrix}, \tag{4.2a}$$

$$\boldsymbol{b} = \begin{pmatrix} -2x^2e^x\left(-y^2+y\right)(2y-1)(x-1)^2, \\ -xy^2e^x\left(x(x+3)-2\right)(x-1)(y-1)^2 \end{pmatrix}, \tag{4.2b}$$

$$p = p_0 \sin(\pi x)\sin(\pi y), \tag{4.2c}$$

$$r = 0, \tag{4.2d}$$

with the prescribed fields $\boldsymbol{w} = \boldsymbol{u}$ and $\boldsymbol{d} = \boldsymbol{b}$, and a constant p_0. Table 4.5 shows the convergence rates for each local variable and the L^∞-norm of the divergence

Two-dimensions

Total number of MPI processes

elem. #	$k=1$	$k=2$	$k=3$	$k=4$
2	1	1	1	1
8	1	1	1	1
32	2	2	2	2
128	2	2	2	2
512	4	4	4	4

Wall-clock time of linear solver in the HDG method (sec)

elem. #	$k=1$	$k=2$	$k=3$	$k=4$
2	0.01	0.01	0.01	0.01
8	0.01	0.01	0.01	0.01
32	0.01	0.02	0.02	0.02
128	0.03	0.04	0.06	0.09
512	0.06	0.11	0.17	0.25

Wall-clock time of linear solver in the E-HDG method (sec)

elem. #	$k=1$	$k=2$	$k=3$	$k=4$
2	0.01	0.01	0.01	0.01
8	0.01	0.01	0.01	0.01
32	0.01	0.01	0.02	0.02
128	0.02	0.03	0.05	0.07
512	0.03	0.08	0.13	0.20

Reduction in computational time of linear solver (%)

elem. #	$k=1$	$k=2$	$k=3$	$k=4$
2	0.00	0.00	0.00	0.00
8	0.00	0.00	0.00	0.00
32	0.00	-50.00	0.00	0.00
128	-33.33	-25.00	-16.67	-22.22
512	-50.00	-27.27	-23.53	-20.00

Three-dimensions

Total number of MPI processes

elem. #	$k=1$	$k=2$	$k=3$	$k=4$
6	1	1	1	2
48	1	2	2	2
364	2	4	4	8
3072	2	8	8	16
24576	**4**	16	16	32

Wall-clock time of linear solver in the HDG method (sec)

elem. #	$k=1$	$k=2$	$k=3$	$k=4$
6	0.01	0.05	0.11	0.42
48	0.04	0.13	0.83	0.98
364	0.41	1.26	3.51	5.93
3072	7.32	14.9	61.91	106.37
24576	**156.51**	419.73	-	-

Wall-clock time of linear solver in the E-HDG method (sec)

elem. #	$k=1$	$k=2$	$k=3$	$k=4$
6	0.01	0.03	0.09	0.17
48	0.02	0.07	1.2	0.55
364	0.09	0.41	1.17	2.75
3072	0.97	3.52	16.48	37.67
24576	**13.08**	66.88	414.78	940.11

Reduction in computational time of linear solver (%)

elem. #	$k=1$	$k=2$	$k=3$	$k=4$
6	0.00	-40.00	-18.18	-59.52
48	-50.00	-46.15	44.58	-43.88
364	-78.05	-67.46	-66.67	-53.63
3072	-86.75	-76.38	-73.38	-64.59
24576	**-91.64**	-84.07	-	-

Table 4.3: The summary of computational time (the averaged maximum of wall-clock time over five runs of identical setting, among all MPI processes) taken by the linear solver for solving the two- and three-dimensional problems using E-HDG and HDG methods with the discretization given in (3.7)-(3.11). The two-dimensional problem is the one presented in Section 4.2.1 with $\mathrm{Re} = \mathrm{Rm} = 1$ and the three-dimensional problem is the one presented in Section 4.2.3 with $\mathrm{Re} = \mathrm{Rm} = 1$. Note that k denotes the degree of approximation and "elem. #" indicates the number of elements used in a given mesh.

errors, with the corresponding convergence plots in Figure 4.2. Examining Table 4.5 suggests that the increment in Re and Rm improves the convergence rates of some local variables in this problem, notably $\boldsymbol{L}_h$, $\boldsymbol{u}_h$, and $\boldsymbol{b}_h$. For a more definitive assessment of convergence rates from the numerical experiment, we focus on the results corresponding to $\mathrm{Re} = \mathrm{Rm} = 1$. In summary, we observe the super convergence rate of $\overline{k} + 3/2$ for r_h, the optimal convergence rates of $k+1$ for $\boldsymbol{u}_h, \boldsymbol{b}_h$, the optimal convergence rate of $\overline{k}+1$ for p_h, and sub-optimal convergence rates of k for $\boldsymbol{L}_h, \boldsymbol{J}_h$.

To numerically assess the pressure robustness of our method, we intentionally perturb the pressure solution. The test is carried out on two different meshes, one with 32 elements and another one with 512 elements, using polynomial degree $k = 2$ for both and a wide range of p_0 values. The results of this study are presented in Table 4.6. It is observed from the table that the L^2-errors of all local variables including the velocity and magnetic fields are independent of p_0 regardless of which mesh is used. The observation implies that these errors do not depend on the pressure field and hence our method could be pressure robust. A particularly noteworthy discovery is the independence of the magnetic field error from the pressure field, a phenomenon previously observed in [47] as well. Plausible reasoning for this observation may stem

Two-dimensions

Total number of MPI processes

elem. #	$k=1$	$k=2$	$k=3$	$k=4$
2	1	1	1	1
8	1	1	1	1
32	2	2	2	2
128	2	2	2	2
512	4	4	4	4

Wall-clock time of assembly & reconstruction in the HDG method (sec)

elem. #	$k=1$	$k=2$	$k=3$	$k=4$
2	0.01	0.02	0.06	0.17
8	0.02	0.08	0.24	0.68
32	0.03	0.16	0.48	1.37
128	0.12	0.63	1.92	5.45
512	0.25	1.28	3.84	11.04

Wall-clock time of assembly & reconstruction in the E-HDG method (sec)

elem. #	$k=1$	$k=2$	$k=3$	$k=4$
2	0.01	0.03	0.06	0.17
8	0.02	0.08	0.24	0.68
32	0.03	0.16	0.48	1.37
128	0.12	0.63	1.91	5.43
512	0.24	1.28	3.85	11.01

Reduction in computational time of assembly & reconstruction (%)

elem. #	$k=1$	$k=2$	$k=3$	$k=4$
2	0.00	50.00	0.00	0.00
8	0.00	0.00	0.00	0.00
32	0.00	0.00	0.00	0.00
128	0.00	0.00	-0.52	-0.37
512	-4.00	0.00	0.26	-0.27

Three-dimensions

Total number of MPI processes

elem. #	$k=1$	$k=2$	$k=3$	$k=4$
6	1	1	1	2
48	1	2	2	2
364	2	4	4	8
3072	2	8	8	16
24576	**4**	16	16	32

Wall-clock time of assembly & reconstruction in the HDG method (sec)

elem. #	$k=1$	$k=2$	$k=3$	$k=4$
6	0.15	1.77	10.95	24.62
48	1.13	6.91	43.96	196.12
364	4.54	28.21	179.37	406.84
3072	36.58	112.53	721.29	1620.16
24576	**146.97**	460.14	-	-

Wall-clock time of assembly & reconstruction in the E-HDG method (sec)

elem. #	$k=1$	$k=2$	$k=3$	$k=4$
6	0.15	1.74	10.93	24.89
48	1.12	6.86	43.82	198.3
364	4.56	28.08	181.27	401.64
3072	36.94	113.67	723.29	1612.38
24576	**145.51**	456.01	2926.25	6533.66

Reduction in computational time of assembly & reconstruction (%)

elem. #	$k=1$	$k=2$	$k=3$	$k=4$
6	0.00	-1.69	-0.18	1.10
48	-0.88	-0.72	-0.32	1.11
364	0.44	-0.46	1.06	-1.28
3072	0.98	1.01	0.28	-0.48
24576	**-0.99**	-0.90	-	-

Table 4.4: The summary of computational time (the averaged maximum of wall-clock time over five runs of identical setting, among all MPI processes) taken by assembly execution and local reconstruction for solving the two- and three-dimensional problems using E-HDG and HDG methods with the discretization given in (3.7)-(3.11). The two-dimensional problem is the one presented in Section 4.2.1 with $\mathrm{Re} = \mathrm{Rm} = 1$ and the three-dimensional problem is the one presented in Section 4.2.3 with $\mathrm{Re} = \mathrm{Rm} = 1$. Note that k denotes the degree of approximation and "elem. #" indicates the number of elements used in a given mesh.

from the absence of the pressure field in the magnetic induction equation presented in (3.1c).

4.2.2. Two-dimensional singular manufactured solution. To assess the robustness of our E-HDG scheme, we apply it to a problem where a strong singularity exists on the boundary. This example illustrates the convergence of the E-HDG scheme using a manufactured solution with a singularity (similar to the example in Section 5.2 of [57] and Section 5.3 of [69]). In particular, we consider a nonconvex domain given by $\Omega = (-1,1)\times(-1,1)\backslash[0,1)\times(-1,0]$. We take $\mathrm{Re} = \mathrm{Rm} = \kappa = 1$, $\boldsymbol{w} = \boldsymbol{0}$, and $\boldsymbol{d} = (-1,1)$. We pick $\boldsymbol{g}$ and $\boldsymbol{f}$ such that the analytical solution of

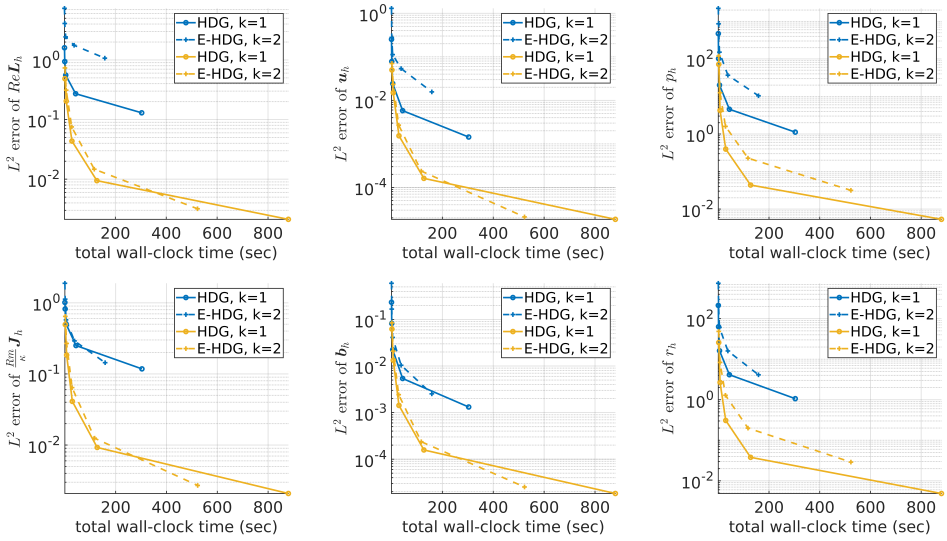

Fig. 4.1: Illustration of Table 4.2 for $k = 1, 2$ with the inclusion of the accuracy of the approximation to different variables.

$\mathrm{Re} = \mathrm{Rm} = 1, \kappa = 1$

	$\mathrm{Re}\boldsymbol{L}_h$	$\boldsymbol{u}_h$	p_h	$\frac{\mathrm{Rm}}{\kappa}\boldsymbol{J}_h$	$\boldsymbol{b}_h$	r_h	$\|\nabla\cdot\boldsymbol{u}_h\|_\infty$	$\|\nabla\cdot\boldsymbol{b}_h\|_\infty$
$k=1$	1.02	2.29	1.12	1.20	2.40	1.96	3.85E-15	4.06E-15
$k=2$	2.02	3.08	2.21	2.28	3.06	2.73	3.44E-14	2.71E-14
$k=3$	3.04	4.06	3.17	3.35	4.03	3.75	7.94E-14	8.45E-14
$k=4$	4.03	5.08	4.28	4.51	4.91	4.79	2.90E-13	4.55E-13
$\mathrm{Re} = \mathrm{Rm} = 1000, \kappa = 1$								
$k=1$	1.29	1.34	0.99	1.36	1.46	0.65	4.30E-15	2.54E-15
$k=2$	2.93	4.05	2.02	3.01	4.14	2.40	2.50E-14	2.17E-14
$k=3$	3.98	5.28	3.02	3.85	5.18	3.81	1.35E-12	1.07E-13
$k=4$	4.16	5.21	4.00	4.17	5.20	4.39	2.67E-12	2.22E-12

Table 4.5: Convergence rates of all local variables and divergence errors of velocity and magnetic fields for the E-HDG method applied to solve the two-dimensional problem with a smooth manufactured solution given in (4.2) with $p_0 = 1$. The corresponding results are also presented in Figure 4.2. In this table, the convergence rates are evaluated at the last two data sets and the divergence errors are evaluated at the last data set.

(3.2)-(3.4) has the form

$$\boldsymbol{u} = \begin{pmatrix} \rho^\lambda \left[(1+\lambda)\sin(\phi)\psi(\phi) + \cos(\phi)\psi'(\phi)\right], \\ \rho^\lambda \left[-(1+\lambda)\cos(\phi)\psi(\phi) + \sin(\phi)\psi'(\phi)\right] \end{pmatrix}, \tag{4.3a}$$

$$\boldsymbol{b} = \nabla\left(\rho^{2/3}\sin\left(\frac{2\phi}{3}\right)\right), \tag{4.3b}$$

$$p = -\rho^{\lambda-1}\frac{(1+\lambda)^2\psi'(\phi) + \psi'''(\phi)}{1-\lambda}, \tag{4.3c}$$

$$r = 0, \tag{4.3d}$$

p_0	$\mathrm{Re}\,\|\boldsymbol{L}-\boldsymbol{L}_h\|_0$	$\|\boldsymbol{u}-\boldsymbol{u}_h\|_0$	$\|p-p_h\|_0$	$\frac{\mathrm{Rm}}{\kappa}\|\boldsymbol{J}-\boldsymbol{J}_h\|_0$	$\|\boldsymbol{b}-\boldsymbol{b}_h\|_0$	$\|r-r_h\|_0$	$\|\nabla\cdot\boldsymbol{u}_h\|_\infty$	$\|\nabla\cdot\boldsymbol{b}_h\|_\infty$
32 elements in total, $h\approx 1.46E-1$								
1	2.09E-2	1.27E-3	5.57E-2	1.67E-2	9.66E-4	3.97E-2	7.15E-16	7.49E-16
10	2.09E-2	1.27E-3	2.02E-1	1.67E-2	9.66E-4	3.97E-2	1.40E-15	6.11E-16
25	2.09E-2	1.27E-3	4.90E-1	1.67E-2	9.66E-4	3.97E-2	2.78E-15	6.66E-16
100	2.09E-2	1.27E-3	1.95	1.67E-2	9.66E-4	3.97E-2	1.03E-14	6.38E-16
512 elements in total, $h\approx 3.66E-2$								
1	1.27E-3	1.09E-5	2.30E-3	7.48E-4	1.07E-5	1.40E-3	4.44E-15	3.77E-15
10	1.27E-3	1.09E-5	1.26E-2	7.48E-4	1.07E-5	1.40E-3	7.41E-15	3.77E-15
25	1.27E-3	1.09E-5	3.11E-2	7.48E-4	1.07E-5	1.40E-3	1.73E-14	4.05E-15
100	1.27E-3	1.09E-5	1.24E-1	7.48E-4	1.07E-5	1.40E-3	7.92E-14	4.11E-15

Table 4.6: The errors in the local variables for the smooth manufactured solution given in (4.2) for meshes of 32 and 512 elements, a polynomial degree of $k=2$, and a range of p_0 values. The physical parameters are set to be $\mathrm{Re}=\mathrm{Rm}=1$ and $\kappa=1$.

where

$$\psi(\phi)=\cos(\lambda\omega)\left[\frac{\sin((1+\lambda)\phi)}{1+\lambda}-\frac{\sin((1-\lambda)\phi)}{1-\lambda}\right]-\cos((1+\lambda)\phi)+\cos((1-\lambda)\phi),$$

$$\omega=\frac{3\pi}{2},\quad \lambda\approx 0.54448373678246,\quad \phi\in\left[0,\frac{3\pi}{2}\right].$$

For this problem, it is known that $\boldsymbol{u}\in\left[H^{1+\lambda}(\Omega)\right]^2$, $p\in H^{\lambda}(\Omega)$, and $\boldsymbol{b}\in\left[H^{2/3}(\Omega)\right]^2$, and the solution contains magnetic and hydrodynamic singularities that are among the strongest singularities [57] right at the origin. The exact solution is illustrated in the first column of Figure 4.4. It can be observed that singularity is located at the origin for $\boldsymbol{b}$ and p. While u is relatively smooth, its derivative is singular at the origin.

A sequence of unstructured meshes is used to test the convergence of the numerical solution. Figure 4.3 demonstrates the coarsest mesh and a couple of refined meshes that are used in the convergence test. The numerical solution and the absolute error which are obtained on the finest mesh with approximation order $k=4$ are presented in Figure 4.4 as well.

Convergence results for this problem are summarized in Table 4.7 and illustrated in Figure 4.5. For the fluid variables $\boldsymbol{L}_h$, $\boldsymbol{u}_h$, and p_h, we observe convergence rates of approximately 2/3. In the case of magnetic variables, namely $\boldsymbol{J}_h$, $\boldsymbol{b}_h$, and r_h, the observed convergence rates are approximately 1/5, 2/3, and 1/3 respectively. Compared to the result presented in [69], the convergence rates of the fluid variables are lower, while the ones of the magnetic variables are similar. Remarkably, despite the accuracy challenges, divergence errors in both velocity and magnetic fields remain close to machine zero in this singular test case.

4.2.3. Three-dimensional smooth manufactured solution. We now apply our E-HDG method to a three-dimensional problem on structured tetrahedron meshes. Note that our well-posedness analysis is still valid for this case. We set $\Omega=(0,1)\times(0,1)\times(0,1)$ and take $\mathrm{Re}=\mathrm{Rm}\in\{1,1000\}$ and $\kappa=1$. For this test case, we choose

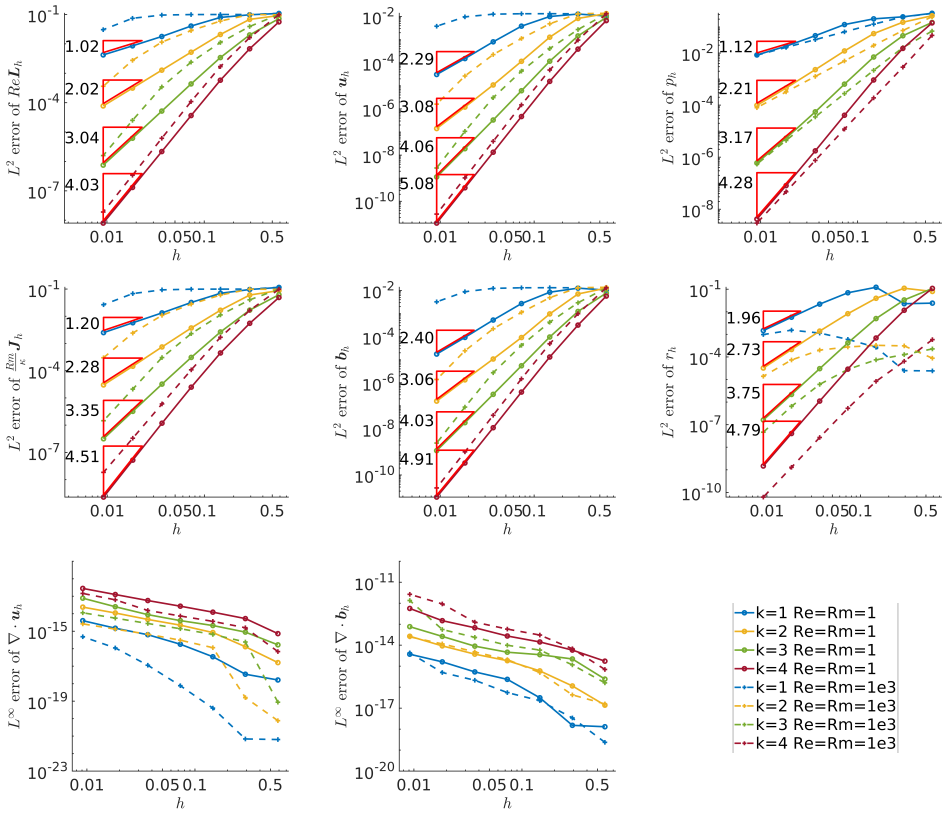

Fig. 4.2: Convergence histories of all local variables and divergence errors for the E-HDG method applied to solve the two-dimensional problem with a smooth manufactured solution given in (4.2) where we set $p_0 = 1$. Only the convergence rates for $\mathrm{Re} = \mathrm{Rm} = 1$ are presented here.

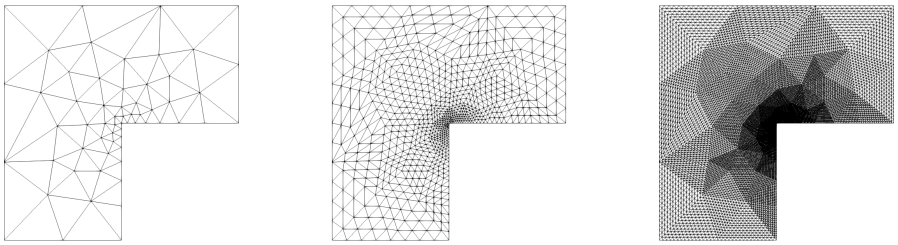

Fig. 4.3: The meshes used in Section 4.2.2. The coarsest mesh is presented in the first column. In the second column, the mesh that undergoes two-times uniform refinement is presented. The finest mesh is shown in the third column and is obtained by four-times uniform refinement.

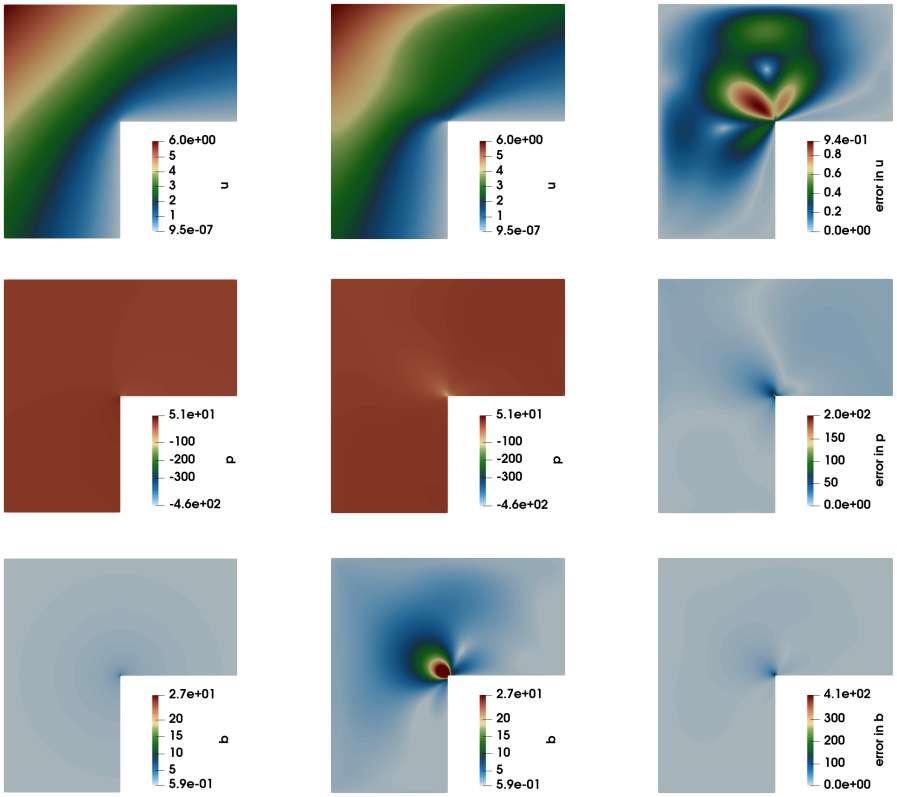

Fig. 4.4: The contour plots of the exact solution (the first column), the numerical solution (the second column), and the error (the third column). The magnitudes of the quantities are presented and all results are obtained by solving the two-dimensional problem with a manufactured solution given in (4.3) where a strong singularity exists in the magnetic field.

$\mathrm{Re} = \mathrm{Rm} = \kappa = 1$

	$\mathrm{Re}\boldsymbol{L}_h$	$\boldsymbol{u}_h$	p_h	$\frac{\mathrm{Rm}}{\kappa}\boldsymbol{J}_h$	$\boldsymbol{b}_h$	r_h	$\|\nabla\cdot\boldsymbol{u}_h\|_\infty$	$\|\nabla\cdot\boldsymbol{b}_h\|_\infty$
$k=1$	0.68	0.68	0.70	0.08	0.71	0.29	8.82e-12	4.22e-10
$k=2$	0.71	0.74	0.76	0.17	0.71	0.31	2.06e-11	4.06e-09
$k=3$	0.60	0.65	0.69	0.33	0.58	0.40	6.25e-11	1.46e-08
$k=4$	0.51	0.54	0.56	0.42	0.51	0.44	1.95e-10	3.82e-08

Table 4.7: Convergence rates of all local variables and divergence errors of velocity and magnetic fields for the E-HDG method applied to solve the two-dimensional problem with a singular manufactured solution given in (4.3). The corresponding results are also presented in Figure 4.5. In this table, the convergence rates are evaluated at the last two data sets and the divergence errors are evaluated at the last data set.

the forcing function such that the exact solution is given by

$$\boldsymbol{u} = \begin{pmatrix} -\left(y\cos\left(y\right)+\sin y\right)e^x, \\ y\sin\left(y\right)e^x-\left(z\cos\left(z\right)+\sin\left(z\right)\right)e^y, \\ z\sin\left(z\right)e^y \end{pmatrix}, \tag{4.4a}$$

$$\boldsymbol{b} = \boldsymbol{u} \tag{4.4b}$$

$$p = p_0\left(2e^x\sin\left(y\right)z^2-\left(\frac{-2}{3}(e\cos\left(1\right)-\cos\left(1\right)-e+1\right)\right) \tag{4.4c}$$

$$r = 0 \tag{4.4d}$$

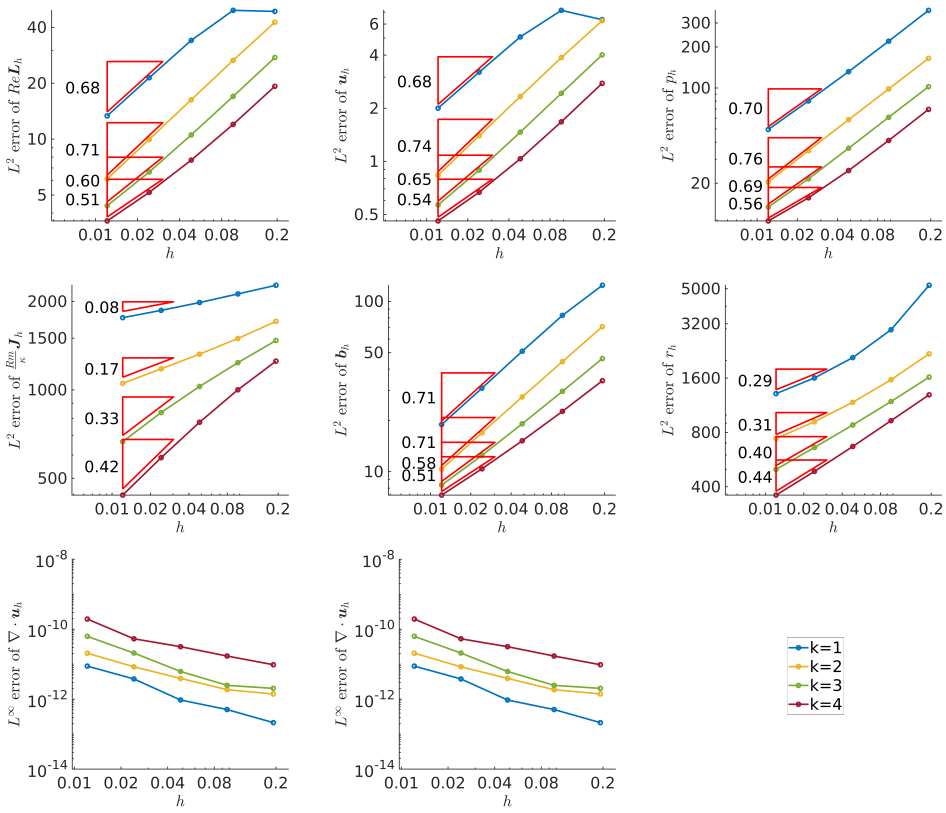

Fig. 4.5: Convergence histories of all local variables and divergence errors for the E-HDG method applied to solve the two-dimensional problem with a manufactured solution given in (4.3) where a strong singularity exists in the magnetic field.

with the prescribed fields $\boldsymbol{w} = \boldsymbol{u}$ and $\boldsymbol{d} = \boldsymbol{b}$, and a constant p_0. Table 4.8 summarizes the convergence rates of all local variables and shows the L^∞-norm of the divergence errors. The corresponding convergence histories are shown in Figure 4.6. Similar to the two-dimensional smooth testing case presented in Section 4.2.1, we observed that the convergence rates are affected by Re and Rm here as well, but in an adverse manner. The effect is evident for $\boldsymbol{L}_h$, $\boldsymbol{u}_h$ and $\boldsymbol{b}_h$. We present the convergence rates for the case $\mathrm{Re} = \mathrm{Rm} = 1$. As can be seen, p_h and r_h exhibit superconvergence with a rate of $\overline{k} + 3/2$, and the convergence rates of $\boldsymbol{u}_h$ and $\boldsymbol{b}_h$ are optimal with $k + 1$. For $\boldsymbol{L}_h$ and $\boldsymbol{J}_h$, the convergence rate is, however, suboptimal with k. The conclusion is consistent with the one made in Section 4.2.1 where the two-dimensional smooth manufactured solution is applied.

The numerical assessment of the pressure robustness of our method is also carried out for this manufactured solution. The examination is conducted by perturbing the solution in pressure on two meshes, one consisting of 48 elements and the other with 24576 elements, with $k = 2$ and various values of p_0. Table 4.9 details the results. Similar to the two-dimensional case presented in Table 4.6, the L^2-errors in velocity and magnetic field are independent of pressure on different meshes.

$\mathrm{Re} = \mathrm{Rm} = 1, \kappa = 1$

	$\mathrm{Re}\boldsymbol{L}_h$	$\boldsymbol{u}_h$	p_h	$\frac{\mathrm{Rm}}{\kappa}\boldsymbol{J}_h$	$\boldsymbol{b}_h$	r_h	$\|\nabla\cdot\boldsymbol{u}_h\|_\infty$	$\|\nabla\cdot\boldsymbol{b}_h\|_\infty$
$k=1$	0.72	1.78	1.81	1.02	2.04	1.95	6.19E-13	2.11E-13
$k=2$	2.21	3.50	2.85	2.21	3.23	2.79	1.41E-12	1.29E-12
$k=3$	3.08	3.99	3.66	3.22	4.19	3.75	9.07E-10	1.96E-11
$k=4$	4.22	5.23	4.73	4.24	5.23	4.70	3.66E-09	8.06E-11
$\mathrm{Re} = \mathrm{Rm} = 1000, \kappa = 1$								
$k=1$	0.47	1.38	1.89	0.56	0.77	1.96	5.73E-13	2.13E-13
$k=2$	1.28	2.25	3.01	1.31	2.19	2.93	1.64E-12	1.45E-12
$k=3$	3.64	4.69	3.92	3.77	4.72	3.93	1.46E-09	1.93E-11
$k=4$	3.94	4.22	4.91	4.03	4.29	5.49	5.55E-09	5.94E-09

Table 4.8: Convergence rates of all local variables and divergence errors of velocity and magnetic fields for the E-HDG method applied to solve the three-dimensional problem with a smooth manufactured solution given in (4.4) where we set $p_0 = 1$. The corresponding results are also presented in Figure 4.6. In this table, the convergence rates are evaluated at the last two data sets and the divergence errors are evaluated at the last data set.

48 elements in total, $h \approx 1.06E-1$

p_0	$\mathrm{Re}\,\|\boldsymbol{L}-\boldsymbol{L}_h\|_0$	$\|\boldsymbol{u}-\boldsymbol{u}_h\|_0$	$\|p-p_h\|_0$	$\frac{\mathrm{Rm}}{\kappa}\|\boldsymbol{J}-\boldsymbol{J}_h\|_0$	$\|\boldsymbol{b}-\boldsymbol{b}_h\|_0$	$\|r-r_h\|_0$	$\|\nabla\cdot\boldsymbol{u}_h\|_\infty$	$\|\nabla\cdot\boldsymbol{b}_h\|_\infty$
1	7.52E-2	2.69E-3	1.59	6.42E-2	2.42E-3	1.29	2.42E-13	2.19E-13
10	7.52E-2	2.69E-3	5.99	6.42E-2	2.42E-3	1.29	2.99E-13	2.48E-13
25	7.52E-2	2.69E-3	15.57	6.42E-2	2.42E-3	1.29	3.09E-13	2.53E-13
100	7.52E-2	2.69E-3	64.09	6.42E-2	2.42E-3	1.29	2.89E-13	2.60E-13
24576 elements in total, $h \approx 2.64E-2$								
1	3.19E-3	2.10E-5	3.16E-2	2.70E-3	2.53E-5	2.90E-2	1.40E-12	1.43E-12
10	3.19E-3	2.10E-5	5.83	2.70E-3	2.53E-5	2.90E-2	1.40E-12	1.31E-12
25	3.19E-3	2.10E-5	15.55	2.70E-3	2.53E-5	2.90E-2	1.41E-12	1.22E-12
100	3.19E-3	2.10E-5	64.13	2.70E-3	2.53E-5	2.90E-2	1.32E-12	1.44E-12

Table 4.9: The errors in the local variables for the smooth manufactured solution given in (4.4) for meshes of 48 and 24576 elements, a polynomial degree of $k = 2$, and a range of p_0 values. We set $\mathrm{Re} = \mathrm{Rm} = 1$ and $\kappa = 1$.

4.3. Nonlinear examples. To verify our nonlinear solver, we conducted several numerical experiments and studied the accuracy and convergence. The first example is the two-dimensional smooth manufactured solution, the second one is the so-called Hartmann flow problem, and the last one is the three-dimensional smooth manufactured solution.

4.3.1. Two-dimensional smooth manufactured solution. Our first numerical experiment for the nonlinear solver is a steady manufactured solution. In particular, we use the same solution presented in Section 4.2.1 to investigate the convergence. The results are presented in Table 4.10 and are illustrated in Figure 4.7. The observed convergence rates are almost the same as the rates observed in the linear problem presented in Section 4.2.1. Moreover, the divergence errors also exhibit the same order of magnitude. Finally, the number of iterations needed by the Picard iterative process is reported in Table 4.11 where the user-defined tolerance ε is set to be $1E-10$ for $k = 1, 2$ and $2E-10$ for $k = 3, 4$.

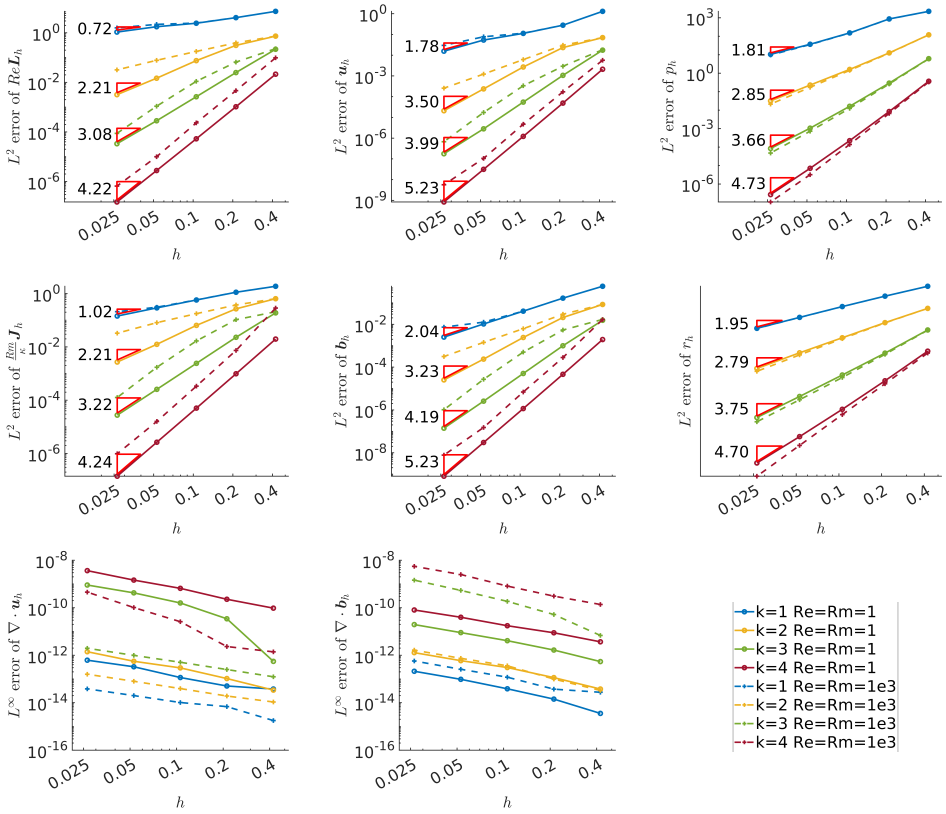

Fig. 4.6: Convergence histories of all local variables and divergence errors for the E-HDG method applied to solve the three-dimensional problem with a smooth manufactured solution given in (4.4) where we set $p_0 = 1$. Only the convergence rates for $\mathrm{Re} = \mathrm{Rm} = 1$ are presented here.

4.3.2. Two-dimensional Hartmann flow. We next consider the Hartmann channel flow, a generalization of the classic plane Poiseuille problem to the setting of the incompressible visco-resistive MHD. In this problem, a conducting incompressible fluid (liquid metal, for example) in a domain $(-\infty, \infty) \times (-l_0, l_0) \times (-\infty, \infty)$ (bounded by infinite parallel plates in the x_2 direction) is driven by a uniform pressure gradient $G := -\frac{\partial p}{\partial x_1}$ in the x_1 direction, and is subject to a uniform external magnetic field b_0 in the x_2 direction. In addition, we enforce no-slip boundary conditions on the x_2 boundaries and assume the infinite parallel plates are perfectly insulating. The resulting flow pattern admits an analytical solution that is one-dimensional in nature. In this numerical study, we consider the simulation of Hartmann flow in a two-dimensional domain $\Omega = (0, 0.025) \times (-1, 1)$. If we define the characteristic velocity as $u_0 := \sqrt{Gl_0/\rho}$ and consider the driving pressure gradient G as a forcing term (incorporated in $\boldsymbol{g}$), the nondimensionalized solution with $\boldsymbol{g} = (1, 0)$, $\boldsymbol{f} = \boldsymbol{0}$ takes the

$\mathrm{Re} = \mathrm{Rm} = 1, \kappa = 1$

	$\mathrm{Re}\boldsymbol{L}_h$	$\boldsymbol{u}_h$	p_h	$\frac{\mathrm{Rm}}{\kappa}\boldsymbol{J}_h$	$\boldsymbol{b}_h$	r_h	$\|\nabla\cdot\boldsymbol{u}_h\|_\infty$	$\|\nabla\cdot\boldsymbol{b}_h\|_\infty$
$k=1$	1.02	2.29	1.12	1.20	2.40	1.96	4.02E-15	3.72E-15
$k=2$	2.02	3.08	2.21	2.28	3.06	2.73	2.39E-14	2.66E-14
$k=3$	3.04	4.06	3.17	3.35	4.03	3.75	7.75E-14	7.65E-14
$k=4$	4.03	5.08	4.28	4.51	4.91	4.79	2.81E-13	5.65E-13
$\mathrm{Re} = \mathrm{Rm} = 1000, \kappa = 1$								
$k=1$	1.27	1.35	0.99	1.38	1.47	0.65	2.69E-15	2.83E-15
$k=2$	2.93	4.04	2.02	3.01	4.14	2.40	2.61E-14	2.35E-14
$k=3$	3.98	5.28	3.02	3.85	5.18	3.81	1.13E-12	1.10E-13
$k=4$	4.16	5.20	4.00	4.17	5.20	4.39	2.78E-12	1.73E-12

Table 4.10: Convergence rates of all local variables and divergence errors of velocity and magnetic fields for the nonlinear solver applied to solve the two-dimensional problem with a smooth manufactured solution given in (4.2) where we set $p_0 = 1$. The corresponding results are also presented in Figure 4.7. In this table, the convergence rates are evaluated at the last two data sets and the divergence errors are evaluated at the last data set.

$Re = Rm = 1, \kappa = 1$

	The Picard iteration number			
elem. #	$k=1$	$k=2$	$k=3$	$k=4$
2	3	3	4	4
8	3	4	4	4
32	3	4	3	3
128	4	3	3	2
512	3	3	2	2
2048	3	3	2	1
8192	3	2	2	2

$Re = Rm = 1000, \kappa = 1$

	The Picard iteration number			
elem. #	$k=1$	$k=2$	$k=3$	$k=4$
2	2	2	2	3
8	2	2	23	38
32	2	24	35	25
128	3	33	30	16
512	4	37	26	10
2048	8	36	18	5
8192	24	32	11	6

Table 4.11: The summary of iteration number required by the Picard iterative process of solving the two-dimensional problem with a smooth manufactured solution given in (4.2) where we set $p_0 = 1$. The user-defined tolerance ε is set to be $1E-10$ for $k = 1, 2$ and $2E-10$ for $k = 3, 4$.

form (see, i.e., [88, 89])

$$\boldsymbol{u} = \left(\frac{\mathrm{Re}}{Ha\tanh(Ha)}\left[1 - \frac{\cosh(Ha\cdot y)}{\cosh(Ha)}\right], 0\right), \tag{4.5a}$$

$$\boldsymbol{b} = \left(\frac{1}{\kappa}\left[\frac{\sinh(Ha\cdot y)}{\sinh(Ha)} - y\right], 1\right), \tag{4.5b}$$

$$p = -\frac{1}{2\kappa}\left[\frac{\sinh(Ha\cdot y)}{\sinh(Ha)} - y\right]^2 - p_0, \tag{4.5c}$$

$$r = 0 \tag{4.5d}$$

where $Ha := \sqrt{\kappa \mathrm{ReRm}}$, and p_0 is a constant that enables p to satisfy the zero average pressure condition.

At refinement level l, the domain is divided into $l \times 80l$ squares, each of which is divided into two triangles from top right to bottom left. Figure 4.8 shows the convergence plots with $\mathrm{Re} = \mathrm{Rm} = 7.07$ and $\kappa = 200$ and the corresponding convergence

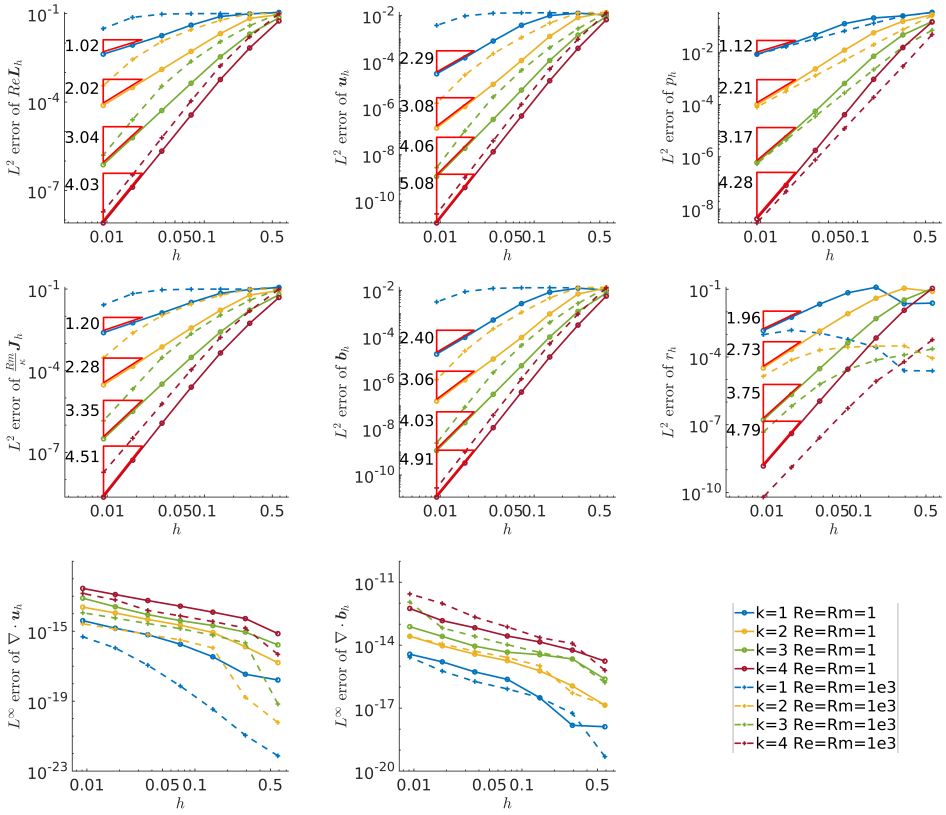

Fig. 4.7: Convergence histories of all local variables and divergence errors for the nonlinear solver applied to solve the two-dimensional problem with a smooth manufactured solution given in (4.2) where we set $p_0 = 1$. Only the convergence rates for $\mathrm{Re} = \mathrm{Rm} = 1$ are presented here.

rates are summarized in Table 4.12. In this example, user-defined tolerance ε is set to be $1E-10$ and the Picard iteration numbers for all cases presented in Figure 4.8 reach 50, which is the maximum allowable number of iterations. However, the computed tolerance TOL is acceptable since it is hovering around $O(1E-9) - O(1E-10)$ for $k = 1$, $O(1E-8) - O(1E-9)$ for $k = 2$, and $O(1E-8)$ for both $k = 3$ and $k = 4$. On the other hand, the convergence rates for $\boldsymbol{L}_h$, $\boldsymbol{u}_h$, p_h, $\boldsymbol{J}_h$, $\boldsymbol{b}_h$, and r_h are observed to be approximately k, $k-1/2$, $\overline{k}+1$, k, $k+1/2$, and $\overline{k}+1$. The observation is consistent with the rates observed in Section 4.2.1 and 4.2.3 except for the ones of the velocity and magnetic fields, which are sub-optimal here.

4.3.3. Three-dimensional smooth manufactured solution. We now turn our attention to a three-dimensional nonlinear problem, demonstrating the convergence of the nonlinear solver utilizing a smooth manufactured solution as outlined in Section 4.2.3. The numerical results are presented in Table 4.13 and visually presented in Figure 4.9. The observed convergence rates are consistent with the rates presented in Section 4.3.3 where a linear problem with the same smooth manufactured solution is solved. Particularly, Table 4.13 closely mirrors the content of Table 4.8. In

$\mathrm{Re} = \mathrm{Rm} = 7.07, \kappa = 200$

	$\mathrm{Re}\boldsymbol{L}_h$	$\boldsymbol{u}_h$	p_h	$\frac{\mathrm{Rm}}{\kappa}\boldsymbol{J}_h$	$\boldsymbol{b}_h$	r_h	$\|\nabla\cdot\boldsymbol{u}_h\|_\infty$	$\|\nabla\cdot\boldsymbol{b}_h\|_\infty$
$k=1$	1.01	3.68	1.01	1.03	1.87	1.26	3.52E-09	5.50E-12
$k=2$	2.08	1.81	2.03	1.96	2.58	1.74	2.95E-08	1.28E-10
$k=3$	3.20	2.59	3.16	3.55	3.64	3.18	1.30E-07	2.90E-10
$k=4$	4.17	3.72	4.13	4.21	4.20	3.96	3.16E-07	7.02E-10

Table 4.12: Convergence rates of all local variables and divergence errors of velocity and magnetic fields for the nonlinear solver applied to solve the two-dimensional Hartmann flow problem that admits the solution given in (4.5). The corresponding results are also presented in Figure 4.8. In this table, the convergence rates are evaluated at the last two data sets and the divergence errors are evaluated at the last data set.

addition, the same order of magnitude is observed for the divergence errors as well.

Table 4.14 concludes the number of iterations needed by the Picard iterative process. In this example, the user-defined tolerance ε is set to be $2E-10$. It is widely known that the Picard solver may not converge consistently, and the success of the iteration is contingent upon the initial guess and the contractive property. Our findings underscore that the convergence of the Picard solver is substantially influenced by the physical parameters Re, Rm, the degree of approximation k, and the mesh refinement. This implies that the contractive property of the linear map $(\boldsymbol{w}, \boldsymbol{d}) \mapsto (\boldsymbol{u}, \boldsymbol{b})$ can be largely affected by these factors. This is not surprising as our analysis in [77] showed the contraction factor is proportional to the initial guess, $\boldsymbol{f}, \boldsymbol{g}, \mathrm{Re}, \mathrm{Rm}/\kappa$ and depends on $\boldsymbol{w}$ and $\boldsymbol{d}$ in a nontrivial nonlinear manner. Specifically, in the testing cases with $\mathrm{Re} = \mathrm{Rm} = 1000$ and $k > 1$, the Picard iteration does not converge when using the initial guess $\boldsymbol{u}_h^0 = \boldsymbol{b}_h^0 = \boldsymbol{0}$. Taking $\mathrm{Re} = \mathrm{Rm} = 1000$, the Picard iteration stalls when $k = 2$ is used on the mesh with 364 elements (TOL stagnates around $O(1E-4)$), $k = 3$ on the mesh with 48 elements (TOL stagnates around $O(1E-4)$), and $k = 4$ on the mesh with 6 elements (TOL stagnates around $O(1E-5)$). Only the case with $k = 1$ exhibits convergence across a sequence of meshes with 6, 48, 364, 3072, and 24576 elements, and the results of this case are presented in both Table 4.13 and Figure 4.9.

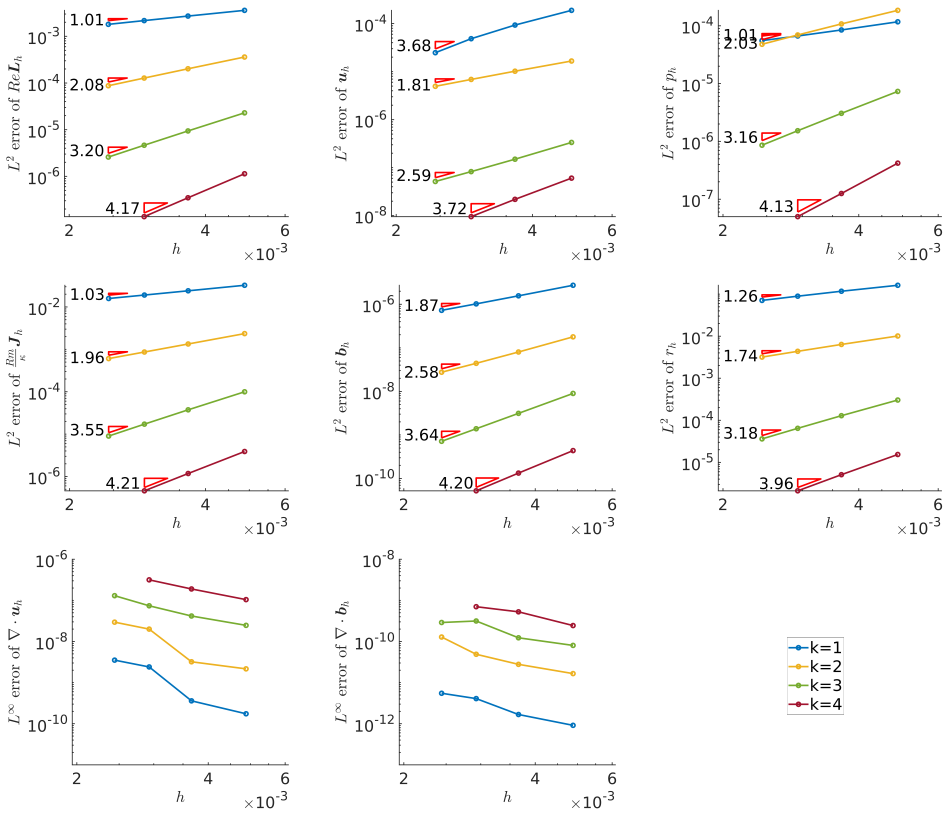

Fig. 4.8: Convergence histories of all local variables and divergence errors for the nonlinear solver applied to solve the two-dimensional Hartmann flow problem that admits the solution given in (4.5).

$\mathrm{Re} = \mathrm{Rm} = 1, \kappa = 1$

	$\mathrm{Re}\boldsymbol{L}_h$	$\boldsymbol{u}_h$	p_h	$\frac{\mathrm{Rm}}{\kappa}\boldsymbol{J}_h$	$\boldsymbol{b}_h$	r_h	$\|\nabla\cdot\boldsymbol{u}_h\|_\infty$	$\|\nabla\cdot\boldsymbol{b}_h\|_\infty$
$k=1$	0.72	1.78	1.81	1.02	2.04	1.95	6.89E-13	2.97E-13
$k=2$	2.21	3.50	2.85	2.21	3.23	2.78	1.37E-12	1.37E-12
$k=3$	3.08	3.99	3.66	3.22	4.19	3.75	9.32E-10	2.07E-11
$k=4$	4.22	5.23	4.73	4.24	5.23	4.70	3.47E-09	8.38E-11
$\mathrm{Re} = \mathrm{Rm} = 1000, \kappa = 1$								
$k=1$	0.47	1.36	1.89	0.57	0.80	1.96	6.08E-13	2.47E-13

Table 4.13: Convergence rates of all local variables and divergence errors of velocity and magnetic fields for the Picard iterations applied to solve the three-dimensional problem with a smooth manufactured solution given in (4.4) where we set $p_0 = 1$. The corresponding results are also presented in Figure 4.9. In this table, the convergence rates are evaluated at the last two data sets and the divergence errors are evaluated at the last data set.

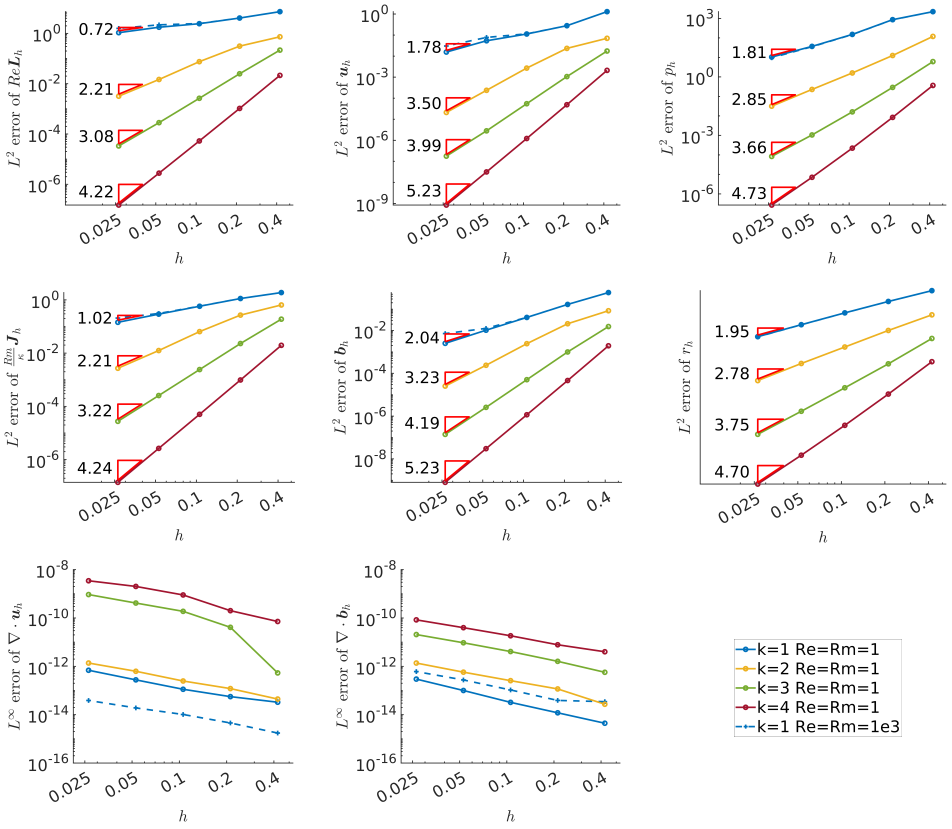

Fig. 4.9: Convergence histories of all local variables and divergence errors for the Picard iterations applied to solve the three-dimensional problem with a smooth manufactured solution given in (4.4) where we set $p_0 = 1$. Only the convergence rates for $\mathrm{Re} = \mathrm{Rm} = 1$ are presented here.

$Re = Rm = 1$, $\kappa = 1$				
The Picard iteration number				
elem. #	$k = 1$	$k = 2$	$k = 3$	$k = 4$
6	3	3	4	5
48	3	5	6	5
364	5	7	5	2
3072	7	6	3	1
24576	8	5	2	1

$Re = Rm = 1000$, $\kappa = 1$				
The Picard iteration number				
elem. #	$k = 1$	$k = 2$	$k = 3$	$k = 4$
6	3	3	-	-
48	3	5	-	-
364	5	-	-	-
3072	10	-	-	-
24576	47	-	-	-

Table 4.14: The summary of iteration number required by the Picard iterative process of solving the two-dimensional problem with a smooth manufactured solution given in (4.4) where we set $p_0 = 1$. In all cases, the user-defined tolerance ε is set to be $2E - 10$. The symbol "-" in the table indicates the failure of the Picard solver, in which not only is the maximum allowable number of iterations reached but also is the computed tolerance TOL generally too large to be acceptable.

5. Conclusion and future work. This paper presents two new divergence-free and $H(div)$-conforming HDG methods for the linearized incompressible viso-resistive MHD equations with well-posedness analysis. Particularly, we have showed that on simplicial meshes, the well-posedness of the proposed approaches can be established by the use of a one-order lower approximation in local variables for the pressure p_h and the Lagrange multiplier r_h, and by appropriately chosen stabilization parameters. One of the motivations for adopting E-HDG in lieu of HDG methods lies in computational gain. Indeed, our experiments have revealed a significant acceleration in the runtime, manifested through the utilization of fewer DOFs in E-HDG, particularly in cases where the linear solver dominates the overall computational time, such as in three dimensions with high-order approximations on fine meshes. Linear problems with both smooth and singular solutions were presented to examine the convergence of the proposed E-HDG method. For problems with smooth solutions, both two- and three-dimensional settings were tested. The numerical convergence rates are shown to be optimal for both velocity and magnetic fields in the regime of low Reynolds number and magnetic Reynolds number. Moreover, the pressure robustness of our method was numerically verified. For the singular solution, the convergence rate is limited by the regularity of the solution. However, the divergence-free property is still guaranteed.

By incorporating the E-HDG discretization into the fixed point Picard iteration, we can solve the nonlinear incompressible viso-resistive MHD equations iteratively. The globally divergence-free property still holds for both the velocity and the magnetic fields. The convergence of the nonlinear solver is investigated through nonlinear problems with smooth solutions. The convergence rates in the tests are almost identical to the ones observed in the linear tests in both two- and three-dimensional settings. Further, divergence errors in both velocity and magnetic fields are indeed observed to be machine zero.

While various aspects of our proposed E-HDG method have been discussed in this paper, there remain several noteworthy issues. Firstly, a rigorous convergence analysis is required, albeit consistent convergence rates for each local variable are observed in numerous numerical experiments in this paper. Secondly, the analysis presented in Section 4.1 may offer an incomplete depiction of the correlation between DOFs and computational time. This limitation arises from the potential inapplicability of the discussed insights to iterative solvers, which are heavily relied upon to address large-scale problems (i.e., see [41, 87, 77] for the discussion about the design of scalable solver in the context of DG, HDG and EDG with application to flow and MHD problems.). Therefore, the development of a scalable iterative approach that demonstrates efficacy across a wide spectrum of Reynolds and magnetic Reynolds numbers is necessary. Finally, it is found that the Picard solver does not converge in some cases on three-dimensional meshes in the regime of high Reynolds number and magnetic Reynolds number. The observation implies that the linear map $(\boldsymbol{w}, \boldsymbol{d}) \mapsto (\boldsymbol{u}, \boldsymbol{b})$ can be largely affected by various factors. Investigating the contraction of this map could provide insights for devising a more robust algorithm. These topics are non-trivial and could each be expanded into individual papers. Thus, we aim to address them in our future research agenda.

Acknowledgments. This research is partially funded by the National Science Foundation awards NSF-OAC-2212442, NSF-2108320, NSF-1808576 and NSF-CAREER-1845799; by the Department of Energy award DE-SC0018147 and DE-SC0022211.

788 REFERENCES

789 [1] O. M. Al-Habahbeh, M. Al-Saqqa, M. Safi, and T. Abo Khater, *Review of magnetohy-*
790 *drodynamic pump applications*, Alexandria Engineering Journal, 55 (2016), pp. 1347–1358,
791 https://doi.org/10.1016/j.aej.2016.03.001.
792 [2] P. R. Amestoy, I. S. Duff, J.-Y. L'Excellent, and J. Koster, *A fully asynchronous multi-*
793 *frontal solver using distributed dynamic scheduling*, SIAM Journal on Matrix Analysis and
794 Applications, 23 (2001), pp. 15–41, https://doi.org/10.1137/S0895479899358194.
795 [3] P. R. Amestoy, A. Guermouche, J.-Y. L'Excellent, and S. Pralet, *Hybrid scheduling*
796 *for the parallel solution of linear systems*, Parallel Computing, 32 (2006), pp. 136–156,
797 https://doi.org/https://doi.org/10.1016/j.parco.2005.07.004. Parallel Matrix Algorithms
798 and Applications (PMAA'04).
799 [4] R. Anderson, J. Andrej, A. Barker, J. Bramwell, J.-S. Camier, J. Cerveny, V. Dobrev,
800 Y. Dudouit, A. Fisher, T. Kolev, W. Pazner, M. Stowell, V. Tomov, I. Akkerman,
801 J. Dahm, D. Medina, and S. Zampini, *MFEM: A modular finite element methods library*,
802 Computers & Mathematics with Applications, 81 (2021), pp. 42–74, https://doi.org/10.
803 1016/j.camwa.2020.06.009.
804 [5] F. Armero and J. C. Simo, *Long-term dissipativity of time-stepping algorithms for an abstract*
805 *evolution equation with applications to the incompressible MHD and Navier-Stokes equa-*
806 *tions*, Computer Methods in Applied Mechanics and Engineering, 131 (1996), pp. 41–90,
807 https://doi.org/10.1016/0045-7825(95)00931-0.
808 [6] D. N. Arnold, *An interior penalty finite element method with discontinuous elements*, SIAM
809 Journal on Numerical Analysis, 19 (1982), pp. 742–760, https://doi.org/10.1137/0719052.
810 Publisher: Society for Industrial and Applied Mathematics.
811 [7] G. A. Baker, *Finite element methods for elliptic equations using nonconforming ele-*
812 *ments*, Mathematics of Computation, 31 (1977), pp. 45–59, https://doi.org/10.1090/
813 S0025-5718-1977-0431742-5.
814 [8] G. A. Baker, W. N. Jureidini, and O. A. Karakashian, *Piecewise solenoidal vector fields*
815 *and the Stokes problem*, SIAM Journal on Numerical Analysis, 27 (1990), pp. 1466–1485.
816 Publisher: Society for Industrial and Applied Mathematics.
817 [9] S. Balay, S. Abhyankar, M. Adams, S. Benson, J. Brown, P. Brune, K. Buschelman,
818 E. Constantinescu, L. Dalcin, A. Dener, V. Eijkhout, J. Faibussowitsch, W. Gropp,
819 V. Hapla, T. Isaac, P. Jolivet, D. Karpeev, D. Kaushik, M. Knepley, F. Kong,
820 S. Kruger, D. May, L. McInnes, R. Mills, L. Mitchell, T. Munson, J. Roman,
821 K. Rupp, P. Sanan, J. Sarich, B. Smith, S. Zampini, H. Zhang, H. Zhang, and
822 J. Zhang, *PETSc/TAO users manual (rev. 3.19)*, 2023, https://doi.org/10.2172/1968587.
823 [10] S. Balay, W. D. Gropp, L. C. McInnes, and B. F. Smith, *Efficient management of paral-*
824 *lelism in object-oriented numerical software libraries*, in Modern Software Tools for Scien-
825 tific Computing, E. Arge, A. M. Bruaset, and H. P. Langtangen, eds., Birkhäuser, 1997,
826 pp. 163–202, https://doi.org/10.1007/978-1-4612-1986-6_8.
827 [11] D. S. Balsara and D. S. Spicer, *A staggered mesh algorithm using high order godunov*
828 *fluxes to ensure solenoidal magnetic fields in magnetohydrodynamic simulations*, Journal of
829 Computational Physics, 149 (1999), pp. 270–292, https://doi.org/10.1006/jcph.1998.6153.
830 [12] F. Bassi, A. Crivellini, D. A. Di Pietro, and S. Rebay, *An artificial compressibility flux*
831 *for the discontinuous Galerkin solution of the incompressible Navier–Stokes equations*,
832 Journal of Computational Physics, 218 (2006), pp. 794–815, https://doi.org/10.1016/j.jcp.
833 2006.03.006.
834 [13] F. Bassi, A. Crivellini, D. A. Di Pietro, and S. Rebay, *An implicit high-order discontinuous*
835 *Galerkin method for steady and unsteady incompressible flows*, Computers & Fluids, 36
836 (2007), pp. 1529–1546, https://doi.org/10.1016/j.compfluid.2007.03.012.
837 [14] P. Bastian and B. Rivière, *Superconvergence and h(div) projection for discon-*
838 *tinuous Galerkin methods*, International Journal for Numerical Methods in
839 Fluids, 42 (2003), pp. 1043–1057, https://doi.org/10.1002/fld.562. _eprint:
840 https://onlinelibrary.wiley.com/doi/pdf/10.1002/fld.562.
841 [15] M. Benzi, G. H. Golub, and J. Liesen, *Numerical solution of saddle point problems*, Acta
842 Numerica, 14 (2005), p. 1–137, https://doi.org/10.1017/S0962492904000212.
843 [16] D. Boffi, F. Brezzi, and M. Fortin, *Mixed Finite Element Methods and Applications*, vol. 44
844 of Springer Series in Computational Mathematics, Springer, 2013, https://doi.org/10.1007/
845 978-3-642-36519-5.
846 [17] M. Bohm, A. R. Winters, G. J. Gassner, D. Derigs, F. Hindenlang, and J. Saur, *An*
847 *entropy stable nodal discontinuous Galerkin method for the resistive MHD equations.*
848 *part i: Theory and numerical verification*, Journal of Computational Physics, 422 (2020),

p. 108076, https://doi.org/10.1016/j.jcp.2018.06.027.
[18] L. Botti and D. A. Di Pietro, *A pressure-correction scheme for convection-dominated incompressible flows with discontinuous velocity and continuous pressure*, Journal of Computational Physics, 230 (2011), pp. 572–585, https://doi.org/10.1016/j.jcp.2010.10.004.
[19] J. U. Brackbill and D. C. Barnes, *The effect of nonzero $\nabla \cdot b$ on the numerical solution of the magnetohydrodynamic equations*, Journal of Computational Physics, 35 (1980), pp. 426–430, https://doi.org/10.1016/0021-9991(80)90079-0.
[20] F. H. Busse, *Magnetohydrodynamics of the earth's dynamo*, Annual Review of Fluid Mechanics, 10 (1978), pp. 435–462, https://doi.org/10.1146/annurev.fl.10.010178.002251. _eprint: https://doi.org/10.1146/annurev.fl.10.010178.002251.
[21] J. Carrero, B. Cockburn, and D. Schötzau, *Hybridized globally divergence-free LDG methods. part i: The Stokes problem*, Mathematics of Computation, 75 (2006), pp. 533–563. Publisher: American Mathematical Society.
[22] A. Cesmelioglu, B. Cockburn, N. C. Nguyen, and J. Peraire, *Analysis of HDG methods for oseen equations*, Journal of Scientific Computing, 55 (2013), pp. 392–431, https://doi.org/10.1007/s10915-012-9639-y.
[23] C. Ciucua, P. Fernandez, A. Christophe, N. C. Nguyen, and J. Peraire, *Implicit hybridized discontinuous Galerkin methods for compressible magnetohydrodynamics*, Elsevier, (2020). Accepted: 2021-10-27T20:36:09Z Publisher: Elsevier BV.
[24] B. Cockburn, *Discontinuous Galerkin methods for computational fluid dynamics*, in Encyclopedia of Computational Mechanics Second Edition, John Wiley & Sons, Ltd, 2017, pp. 1–63, https://doi.org/10.1002/9781119176817.ecm2053. _eprint: https://onlinelibrary.wiley.com/doi/pdf/10.1002/9781119176817.ecm2053.
[25] B. Cockburn, J. Gopalakrishnan, and R. Lazarov, *Unified hybridization of discontinuous Galerkin, mixed, and continuous Galerkin methods for second order elliptic problems*, SIAM Journal on Numerical Analysis, 47 (2009), pp. 1319–1365, https://doi.org/10.1137/070706616. Publisher: Society for Industrial and Applied Mathematics.
[26] B. Cockburn, J. Gopalakrishnan, N. C. Nguyen, J. Peraire, and F.-J. Sayas, *Analysis of HDG methods for stokes flow*, 80, pp. 723–723, https://doi.org/10.1090/S0025-5718-2010-02410-X.
[27] B. Cockburn, G. Kanschat, and D. Schötzau, *A locally conservative LDG method for the incompressible Navier-Stokes equations*, Mathematics of Computation, 74 (2005), pp. 1067–1095. Publisher: American Mathematical Society.
[28] B. Cockburn, G. Kanschat, and D. Schötzau, *A note on discontinuous Galerkin divergence-free solutions of the Navier–Stokes equations*, Journal of Scientific Computing, 31 (2007), pp. 61–73, https://doi.org/10.1007/s10915-006-9107-7.
[29] B. Cockburn, G. Kanschat, and D. Schötzau, *An equal-order DG method for the incompressible Navier-Stokes equations*, Journal of Scientific Computing, 40 (2009), pp. 188–210, https://doi.org/10.1007/s10915-008-9261-1.
[30] B. Cockburn and F.-J. Sayas, *Divergence-conforming HDG methods for Stokes flows*, Mathematics of Computation, 83 (2014), pp. 1571–1598, https://doi.org/10.1090/S0025-5718-2014-02802-0.
[31] P. A. Davidson, *Magnetohydrodynamics in materials processing*, Annual Review of Fluid Mechanics, 31 (1999), pp. 273–300, https://doi.org/10.1146/annurev.fluid.31.1.273. _eprint: https://doi.org/10.1146/annurev.fluid.31.1.273.
[32] P. A. Davidson, *An Introduction to Magnetohydrodynamics*, Cambridge Texts in Applied Mathematics, Cambridge University Press, 2001, https://doi.org/10.1017/CBO9780511626333.
[33] A. Dedner, F. Kemm, D. Kröner, C. D. Munz, T. Schnitzer, and M. Wesenberg, *Hyperbolic divergence cleaning for the MHD equations*, Journal of Computational Physics, 175 (2002), pp. 645–673, https://doi.org/10.1006/jcph.2001.6961.
[34] D. Derigs, A. R. Winters, G. J. Gassner, and S. Walch, *A novel high-order, entropy stable, 3d AMR MHD solver with guaranteed positive pressure*, Journal of Computational Physics, 317 (2016), pp. 223–256, https://doi.org/10.1016/j.jcp.2016.04.048.
[35] J. Douglas and T. Dupont, *Interior penalty procedures for elliptic and parabolic Galerkin methods*, in Computing Methods in Applied Sciences, R. Glowinski and J. L. Lions, eds., Lecture Notes in Physics, Springer, 1976, pp. 207–216, https://doi.org/10.1007/BFb0120591.
[36] H. Elman, D. Silvester, and A. Wathen, *Finite Elements and Fast Iterative Solvers: with Applications in Incompressible Fluid Dynamics*, Oxford University Press, 06 2014, https://doi.org/10.1093/acprof:oso/9780199678792.001.0001.
[37] A. Ern and J.-L. Guermond, *Finite Elements I: Approximation and Interpolation*, vol. 72 of

Texts in Applied Mathematics, Springer International Publishing, 2021, https://doi.org/10.1007/978-3-030-56341-7.

[38] C. R. Evans and J. F. Hawley, *Simulation of magnetohydrodynamic flows: A constrained transport model*, The Astrophysical Journal, 332 (1988), p. 659, https://doi.org/10.1086/166684. ADS Bibcode: 1988ApJ...332..659E.

[39] L. C. Evans, *Partial differential equations*, vol. 19, American Mathematical Society, 2022.

[40] P. Fernandez, N. C. Nguyen, and J. Peraire, *The hybridized discontinuous galerkin method for implicit large-eddy simulation of transitional turbulent flows*, 336, pp. 308–329, https://doi.org/10.1016/j.jcp.2017.02.015.

[41] K. Fidkowski, *Analysis of iterative solvers for hybridized discontinuous Galerkin methods*, in AIAA AVIATION 2021 FORUM, American Institute of Aeronautics and Astronautics, 2021, https://doi.org/10.2514/6.2021-2718. _eprint: https://arc.aiaa.org/doi/pdf/10.2514/6.2021-2718.

[42] C. Forsberg, *The advanced high-temperature reactor: High-temperature fuel, liquid salt coolant, liquid-metal-reactor plant*, Progress in Nuclear Energy, 47 (2005), pp. 32–43, https://doi.org/10.1016/j.pnucene.2005.05.002.

[43] G. Fu, *An explicit divergence-free DG method for incompressible magnetohydrodynamics*, Journal of Scientific Computing, 79 (2019), pp. 1737–1752, https://doi.org/10.1007/s10915-019-00909-2.

[44] J.-F. Gerbeau, *A stabilized finite element method for the incompressible magnetohydrodynamic equations*, Numerische Mathematik, 87 (2000), pp. 83–111, https://doi.org/10.1007/s002110000193.

[45] J.-F. Gerbeau, C. Le Bris, and T. Lelièvre, *Mathematical methods for the magnetohydrodynamics of liquid metals*, Clarendon Press, 2006.

[46] V. Girault and P.-A. Raviart, *Finite Element Methods for Navier-Stokes Equations*, vol. 5 of Springer Series in Computational Mathematics, Springer, 1986, https://doi.org/10.1007/978-3-642-61623-5.

[47] T. A. Gleason, E. L. Peters, and J. A. Evans, *A divergence-conforming hybridized discontinuous Galerkin method for the incompressible magnetohydrodynamics equations*, 2022, https://doi.org/10.48550/arXiv.2201.01906, https://arxiv.org/abs/2201.01906[cs,math].

[48] J. P. H. Goedbloed and S. Poedts, *Principles of Magnetohydrodynamics: With Applications to Laboratory and Astrophysical Plasmas*, Cambridge University Press, 2004, https://doi.org/10.1017/CBO9780511616945.

[49] M. Goossens, *An Introduction to Plasma Astrophysics and Magnetohydrodynamics*, vol. 294 of Astrophysics and Space Science Library, Springer Netherlands, 2003, https://doi.org/10.1007/978-94-007-1076-4.

[50] C. Greif, D. Li, D. Schötzau, and X. Wei, *A mixed finite element method with exactly divergence-free velocities for incompressible magnetohydrodynamics*, Computer Methods in Applied Mechanics and Engineering, 199 (2010), pp. 2840–2855, https://doi.org/10.1016/j.cma.2010.05.007.

[51] M. D. Gunzburger, A. J. Meir, and J. S. Peterson, *On the existence, uniqueness, and finite element approximation of solutions of the equations of stationary, incompressible magnetohydrodynamics*, Mathematics of Computation, 56 (1991), pp. 523–563, https://doi.org/10.1090/S0025-5718-1991-1066834-0.

[52] J. Guzmán, C.-W. Shu, and F. A. Sequeira, *H(div) conforming and DG methods for incompressible Euler's equations*, IMA Journal of Numerical Analysis, 37 (2017), pp. 1733–1771, https://doi.org/10.1093/imanum/drw054.

[53] S. Güzey, B. Cockburn, and H. K. Stolarski, *The embedded discontinuous Galerkin method: application to linear shell problems*, International Journal for Numerical Methods in Engineering, 70 (2007), pp. 757–790, https://doi.org/10.1002/nme.1893. _eprint: https://onlinelibrary.wiley.com/doi/pdf/10.1002/nme.1893.

[54] J. S. Hesthaven and T. Warburton, *Nodal Discontinuous Galerkin Methods*, vol. 54 of Texts in Applied Mathematics, Springer, 2008, https://doi.org/10.1007/978-0-387-72067-8.

[55] T. L. Horváth and S. Rhebergen, *An exactly mass conserving space-time embedded-hybridized discontinuous Galerkin method for the Navier–Stokes equations on moving domains*, Journal of Computational Physics, 417 (2020), p. 109577, https://doi.org/10.1016/j.jcp.2020.109577.

[56] T. L. Horváth and S. Rhebergen, *A conforming sliding mesh technique for an embedded-hybridized discontinuous Galerkin discretization for fluid-rigid body interaction*, International Journal for Numerical Methods in Fluids, 94 (2022), pp. 1784–1809, https://doi.org/10.1002/fld.5127. _eprint: https://onlinelibrary.wiley.com/doi/pdf/10.1002/fld.5127.

[57] P. Houston, D. Schötzau, and X. Wei, *A mixed DG method for linearized incompressible*

magnetohydrodynamics, Journal of Scientific Computing, 40 (2009), pp. 281–314, https://doi.org/10.1007/s10915-008-9265-x.

[58] P. Janhunen, *A positive conservative method for magnetohydrodynamics based on HLL and roe methods*, Journal of Computational Physics, 160 (2000), pp. 649–661, https://doi.org/10.1006/jcph.2000.6479.

[59] V. John, A. Linke, C. Merdon, M. Neilan, and L. G. Rebholz, *On the divergence constraint in mixed finite element methods for incompressible flows*, SIAM Review, 59 (2017), pp. 492–544, https://doi.org/10.1137/15M1047696. Publisher: Society for Industrial and Applied Mathematics.

[60] O. A. Karakashian and W. N. Jureidini, *A nonconforming finite element method for the stationary Navier-Stokes equations*, SIAM Journal on Numerical Analysis, 35 (1998), pp. 93–120. Publisher: Society for Industrial and Applied Mathematics.

[61] B. Klein, F. Kummer, and M. Oberlack, *A SIMPLE based discontinuous Galerkin solver for steady incompressible flows*, Journal of Computational Physics, 237 (2013), pp. 235–250, https://doi.org/10.1016/j.jcp.2012.11.051.

[62] C. Klingenberg, F. Pörner, and Y. Xia, *An efficient implementation of the divergence free constraint in a discontinuous Galerkin method for magnetohydrodynamics on unstructured meshes*, Communications in Computational Physics, 21 (2017), pp. 423–442, https://doi.org/10.4208/cicp.180515.230616a. Publisher: Cambridge University Press.

[63] F. Krause and K.-H. Rädler, *Mean-field magnetohydrodynamics and dynamo theory*, Elsevier, 2016.

[64] A. La Spina and J. Fish, *A superconvergent hybridizable discontinuous Galerkin method for weakly compressible magnetohydrodynamics*, Computer Methods in Applied Mechanics and Engineering, 388 (2022), p. 114278, https://doi.org/10.1016/j.cma.2021.114278.

[65] R. J. Labeur and G. N. Wells, *A Galerkin interface stabilisation method for the advection–diffusion and incompressible Navier–Stokes equations*, Computer Methods in Applied Mechanics and Engineering, 196 (2007), pp. 4985–5000, https://doi.org/10.1016/j.cma.2007.06.025.

[66] R. J. Labeur and G. N. Wells, *Energy stable and momentum conserving hybrid finite element method for the incompressible Navier–Stokes equations*, SIAM Journal on Scientific Computing, 34 (2012), pp. A889–A913, https://doi.org/10.1137/100818583. Publisher: Society for Industrial and Applied Mathematics.

[67] P. L. Lederer, C. Lehrenfeld, and J. Schöberl, *Hybrid discontinuous Galerkin methods with relaxed h(div)-conformity for incompressible flows. part i*, SIAM Journal on Numerical Analysis, 56 (2018), pp. 2070–2094, https://doi.org/10.1137/17M1138078. Publisher: Society for Industrial and Applied Mathematics.

[68] J. J. Lee, S. Shannon, T. Bui-Thanh, and J. N. Shadid, *Analysis of an HDG method for linearized incompressible resistive MHD equations*, 2019, https://doi.org/10.48550/arXiv.1702.05124, https://arxiv.org/abs/1702.05124[math].

[69] J. J. Lee, S. J. Shannon, T. Bui-Thanh, and J. N. Shadid, *Analysis of an HDG method for linearized incompressible resistive MHD equations*, SIAM Journal on Numerical Analysis, 57 (2019), pp. 1697–1722, https://doi.org/10.1137/18M1166729. Publisher: Society for Industrial and Applied Mathematics.

[70] C. Lehrenfeld, *Hybrid discontinuous Galerkin methods for solving incompressible flow problems*, Rheinisch-Westfalischen Technischen Hochschule Aachen, 111 (2010).

[71] C. Lehrenfeld and J. Schöberl, *High order exactly divergence-free hybrid discontinuous Galerkin methods for unsteady incompressible flows*, Computer Methods in Applied Mechanics and Engineering, 307 (2016), pp. 339–361, https://doi.org/10.1016/j.cma.2016.04.025.

[72] F. Li and C.-W. Shu, *Locally divergence-free discontinuous Galerkin methods for MHD equations*, Journal of Scientific Computing, 22 (2005), pp. 413–442, https://doi.org/10.1007/s10915-004-4146-4.

[73] A. Linke, *On the role of the Helmholtz decomposition in mixed methods for incompressible flows and a new variational crime*, Computer Methods in Applied Mechanics and Engineering, 268 (2014), pp. 782–800, https://doi.org/10.1016/j.cma.2013.10.011.

[74] A. Linke and C. Merdon, *Pressure-robustness and discrete Helmholtz projectors in mixed finite element methods for the incompressible Navier–Stokes equations*, Computer Methods in Applied Mechanics and Engineering, 311 (2016), pp. 304–326, https://doi.org/10.1016/j.cma.2016.08.018.

[75] P. Londrillo and L. D. Zanna, *High-order upwind schemes for multidimensional magnetohydrodynamics*, The Astrophysical Journal, 530 (2000), p. 508, https://doi.org/10.1086/308344. Publisher: IOP Publishing.

[76] K. Miyamoto, *Plasma physics for nuclear fusion*, Cambridge, (1980).

[77] S. Muralikrishnan, S. Shannon, T. Bui-Thanh, and J. N. Shadid, *A multilevel block preconditioner for the HDG trace system applied to incompressible resistive MHD*, Computer Methods in Applied Mechanics and Engineering, 404 (2023), p. 115775, https://doi.org/10.1016/j.cma.2022.115775.

[78] N. C. Nguyen, J. Peraire, and B. Cockburn, *An implicit high-order hybridizable discontinuous galerkin method for the incompressible navier–stokes equations*, 230, pp. 1147–1170, https://doi.org/10.1016/j.jcp.2010.10.032.

[79] N. C. Nguyen, J. Peraire, and B. Cockburn, *A class of embedded discontinuous Galerkin methods for computational fluid dynamics*, Journal of Computational Physics, 302 (2015), pp. 674–692, https://doi.org/10.1016/j.jcp.2015.09.024.

[80] J. Peraire, C. Nguyen, and B. Cockburn, *An embedded discontinuous Galerkin method for the compressible Euler and Navier-Stokes equations*, in 20th AIAA Computational Fluid Dynamics Conference, 2011, p. 3228.

[81] E. L. Peters and J. A. Evans, *A divergence-conforming hybridized discontinuous Galerkin method for the incompressible Reynolds-averaged Navier-Stokes equations*, International Journal for Numerical Methods in Fluids, 91 (2019), pp. 112–133, https://doi.org/10.1002/fld.4745. _eprint: https://onlinelibrary.wiley.com/doi/pdf/10.1002/fld.4745.

[82] K. G. Powell, P. L. Roe, T. J. Linde, T. I. Gombosi, and D. L. De Zeeuw, *A solution-adaptive upwind scheme for ideal magnetohydrodynamics*, Journal of Computational Physics, 154 (1999), pp. 284–309, https://doi.org/10.1006/jcph.1999.6299.

[83] W. Qiu and K. Shi, *A mixed DG method and an HDG method for incompressible magnetohydrodynamics*, IMA Journal of Numerical Analysis, 40 (2020), pp. 1356–1389, https://doi.org/10.1093/imanum/dry095.

[84] S. Rhebergen and B. Cockburn, *A space–time hybridizable discontinuous Galerkin method for incompressible flows on deforming domains*, Journal of Computational Physics, 231 (2012), pp. 4185–4204, https://doi.org/10.1016/j.jcp.2012.02.011.

[85] S. Rhebergen and G. N. Wells, *Analysis of a hybridized/interface stabilized finite element method for the Stokes equations*, SIAM Journal on Numerical Analysis, 55 (2017), pp. 1982–2003, https://doi.org/10.1137/16M1083839. Publisher: Society for Industrial and Applied Mathematics.

[86] S. Rhebergen and G. N. Wells, *A hybridizable discontinuous Galerkin method for the Navier–Stokes equations with pointwise divergence-free velocity field*, Journal of Scientific Computing, 76 (2018), pp. 1484–1501, https://doi.org/10.1007/s10915-018-0671-4.

[87] S. Rhebergen and G. N. Wells, *An embedded–hybridized discontinuous Galerkin finite element method for the Stokes equations*, Computer Methods in Applied Mechanics and Engineering, 358 (2020), p. 112619, https://doi.org/10.1016/j.cma.2019.112619.

[88] J. N. Shadid, R. P. Pawlowski, J. W. Banks, L. Chacón, P. T. Lin, and R. S. Tuminaro, *Towards a scalable fully-implicit fully-coupled resistive MHD formulation with stabilized FE methods*, Journal of Computational Physics, 229 (2010), pp. 7649–7671, https://doi.org/10.1016/j.jcp.2010.06.018.

[89] J. N. Shadid, R. P. Pawlowski, E. C. Cyr, R. S. Tuminaro, L. Chacón, and P. D. Weber, *Scalable implicit incompressible resistive MHD with stabilized FE and fully-coupled newton–krylov-AMG*, Computer Methods in Applied Mechanics and Engineering, 304 (2016), pp. 1–25, https://doi.org/10.1016/j.cma.2016.01.019.

[90] F. L. Tabarés, *Present status of liquid metal research for a fusion reactor*, Plasma Physics and Controlled Fusion, 58 (2015), p. 014014, https://doi.org/10.1088/0741-3335/58/1/014014. Publisher: IOP Publishing.

[91] G. Tóth, *The $\nabla\cdot b=0$ constraint in shock-capturing magnetohydrodynamics codes*, Journal of Computational Physics, 161 (2000), pp. 605–652, https://doi.org/10.1006/jcph.2000.6519.

[92] J. Wang and X. Ye, *New finite element methods in computational fluid dynamics by h(div) elements*, SIAM Journal on Numerical Analysis, 45 (2007), pp. 1269–1286, https://doi.org/10.1137/060649227.

[93] M. F. Wheeler, *An elliptic collocation-finite element method with interior penalties*, SIAM Journal on Numerical Analysis, 15 (1978), pp. 152–161, https://doi.org/10.1137/0715010. Publisher: Society for Industrial and Applied Mathematics.

[94] S. Yakovlev, L. Xu, and F. Li, *Locally divergence-free central discontinuous Galerkin methods for ideal MHD equations*, Journal of Computational Science, 4 (2013), pp. 80–91, https://doi.org/10.1016/j.jocs.2012.05.002.